Specialized axon initial segment enables low firing threshold and rapid action potential output in fast-spiking interneurons of the human neocortex

Specialized axon initial segment in human neurons

Emoke Bakos[¶1,2], Ádám Tiszlavicz[¶1], Viktor Szegedi[1,2], Abdennour Douida[1], Szabina Furdan[1], Daphne K. Welter[3], Jonathan M. Landry[3], Balazs Bende[4], Gabor Hutoczki[5], Pal Barzo[6], Gabor Tamas[7], Vladimir Benes[3], Attila Szucs[8], Karri Lamsa*[1,2]

ORCID Identifiers:

Emoke Bakos: https://orcid.org/0009-0001-4790-4352

Adam Tiszlavicz: https://orcid.org/0009-0008-4830-0594

Viktor Szegedi: https://orcid.org/0000-0003-4191-379X

Szabina Furdan: https://orcid.org/0000-0002-8878-0966

Daphne K. Welter: https://orcid.org/0000-0002-2430-2391

Jonathan M. Landry: https://orcid.org/0000-0003-2262-9099

Gabor Hutoczki: https://orcid.org/ 0000-0001-7048-0757

Pal Barzo: https://orcid.org/0000-0001-8717-748X

Gabor Tamas: https://orcid.org/0000-0002-7905-6001

Vladimir Benes: https://orcid.org/0000-0002-0352-2547

Attila Szucs: https://orcid.org/0000-0001-9733-4135

Karri Lamsa: https://orcid.org/0000-0002-4609-1337

Affiliations

[1]Hungarian Center of Excellence for Molecular Medicine Research Group for Human neuron physiology and therapy, Szeged, Hungary

[2]Department of Physiology, Anatomy and Neuroscience, University of Szeged, Szeged, Hungary

[3]European Molecular Biology Laboratory, Heidelberg, Germany

[4]Hungarian Centre of Excellence for Molecular Medicine Research Group for Translational Medicine Development, Szeged, Hungary

[5]Department of Neurosurgery, University of Debrecen Clinical Centre, Debrecen Hungary

[6]Department of Neurosurgery, University of Szeged, Szeged, Hungary

[7]ELKH-SZTE Research Group for Cortical Microcircuits, Department of Physiology, Anatomy and Neuroscience, University of Szeged, Szeged, Hungary

[8]Neuronal Cell Biology Research Group, Eötvös Loránd University, Budapest, Hungary

*Corresponding author

Email: klamsa@bio.u-szeged.hu; karri.lamsa@hcemm.eu (KL)

¶These authors contributed equally to this work.

Abstract

The mammalian brain exhibits notable interspecies variation. Microanatomical and molecular differences in homologous neurons, those with similar locations and developmental origins across species, are best characterized in the neocortical mantle, the center of complex brain functions; however, the purpose of these differences remains unclear. We performed whole-cell microelectrode recordings along with microanatomical and molecular analyses of human fast-spiking parvalbumin (pvalb)-expressing interneurons in neocortical tissue resected during brain surgery, comparing them with similar data obtained from the mouse neocortex. The action potential (AP) firing threshold was lower in human neurons than in mouse neurons. This was due to a deficiency in low-voltage–activated inhibitory Kv1.1 and Kv1.2 potassium channels in the axon initial segment (AIS), a specialized axonal region that determines AP threshold and initiation, in human cells. In contrast, Kv1 ion channels were prominent in mouse neurons. The AIS was also elongated in humans. Computational simulations of fast-spiking interneurons revealed that the human-type AIS lowers the AP threshold and shortens the time lag for AP initiation. We found that the low membrane AP firing threshold in pvalb neurons is closely linked to slow membrane potential kinetics in the soma. Thus, the human AIS supports fast in–fast out circuit function in human pvalb neurons, compensating for electrically slow somatic membrane responses. When formulating therapeutic strategies that involve fast-spiking neurons, it is crucial to take into account the molecular and functional species differences.

Short blurb: Fast-spiking neurons in the human neocortex feature structural and molecular specializations in the axon initial segment that lower firing thresholds and minimize input–output delay.

Introduction

All organs in the body evolved specialized functions to optimally support animal life and vitality. The mammalian brain exhibits interspecies differences not only in volume and cortical convolution but also in nerve cell microstructure and molecular composition [1, 2]. Although the brain comprises homologous neurons, sharing similar locations and developmental origins across species, these cells show species-specific differentiation at the microscale level [3-6]. The purpose of this neuronal specialization across species remains poorly understood [7, 8], although these adaptations likely optimize neural circuit function [9]. Neuron types and their species-specific features are best characterized in the neocortical mantle, the center of complex high-order brain functions [1, 5, 6, 10-19]. Neocortical function has been intensively studied in relation to brain cognitive and behavioral processes in humans and animal models, the latter aiding in elucidating the roles of neuron types in these processes [20-22]. However, studies using resected human brain tissue have revealed various "human-specific" transcriptomic and microstructural features in neocortical neurons [7, 10, 11, 23-31]. Many of these differences likely contribute to species-specific neuronal functions; however, the structure–function relationship remains unclear [12, 16, 17, 19, 30, 32-34].

Distinctive differences in homologous neurons between the rodent and human neocortex include electrical resistivity and the membrane potential level required to trigger action potentials (APs) [25]. Human neocortical excitatory pyramidal neurons exhibit lower input resistance (Rin) and require greater membrane depolarization (i.e., a higher AP firing threshold) to trigger APs compared with rodent neurons [24, 29, 35]. In contrast, inhibitory interneurons in the human neocortex display higher input resistance and a lower AP firing

threshold relative to their rodent counterparts [26, 27]. Prior studies suggest that these interspecies differences also apply to fast-spiking interneurons [28, 31, 36], the principal inhibitory neuron population in the neocortex, characterized by the expression of *parvalbumin* (*PVALB*), the gene encoding pvalb protein [23]. In humans, pvalb neurons exhibit elevated input resistance; therefore, they generate membrane potential (Vm) changes with reduced electric input [28]. For the same reason, Vm changes, such as excitatory synaptic potentials that lead to APs, occur more slowly [28, 31, 36-39]. The delayed Vm response in human fast-spiking neurons, compared with that in their rodent counterparts, appears counterintuitive, as the rapid transformation of excitatory input to AP output (i.e., input–output transformation) is a hallmark of pvalb interneurons, also known as "fast in–fast out" inhibitory circuits [38, 40]. Pvalb interneurons play a crucial role in complex brain functions. They rapidly inhibit other neurons and orchestrate temporally coordinated network activities that underlie cognitive processes. Their ability to rapidly and reliably inhibit other neurons allows them to precisely control local circuits and shape brain network activity. We hypothesize that a low AP threshold coexists with slow membrane potential kinetics in human pvalb neurons to accelerate their operation in these processes.

In the present study, whole-cell electrophysiological recordings in human and mouse *ex vivo* neocortical slices revealed an association between slow somatic Vm changes and a lowered AP generation threshold in pvalb/*PVALB* interneurons. The reduced AP firing threshold in human cells was accompanied by structural and molecular specialization of the axon initial segment (AIS), a speciated axonal structure that initiates APs [41, 42], which is elongated and deficient in inhibitory Kv1 potassium channels in human neurons. Simulations of fast-spiking interneurons with a human-type AIS showed that a reduced AP threshold shortens the latency of AP initiation, enabling human pvalb neurons to function as fast in–fast out circuits despite slower somatic membrane responses [43].

Results

Pvalb interneurons in humans exhibit a lower AP firing threshold

We measured AP firing thresholds in 91 pvalb-expressing fast-spiking interneurons [43] from human neocortical tissue resected during deep-brain surgery in 67 patients (Table S1). The cells were studied using whole-cell clamp recordings in layer 2/3 of acute brain slices sectioned from the frontal (n = 39 cells), temporal (n = 25 cells), and parietal, occipital, or other neocortical regions (n = 27 cells) in male (n = 30) and female (n = 34) patients aged 11–85 years. The neurons were filled with biocytin during recordings and visualized *post hoc* using streptavidin–fluorophore conjugates. All cells were immunopositive for pvalb (n = 79; Fig 1A1–3) or expressed *PVALB* based on mRNA analysis using patch-sequencing following nucleus harvesting (n = 12; Table S1). For comparison, we also investigated pvalb-expressing interneurons in the mouse neocortex (n = 95).

Fig. 1. Lowered AP firing threshold in fast-spiking pvalb interneurons in the human versus mouse neocortex.

(A) AP firing threshold was examined in layer 2/3 interneurons showing a positive immunoreaction for pvalb. (A1) Excitatory Vm steps (incremental amplitude steps under whole cell current–clamp conditions at −70 mV) revealed the AP threshold. (A2) Human neocortex pvalb neurons were visualized postrecording; the soma and dendrites (black) and axon (red) were filled with biocytin and are shown in three merged 50-µm-thick sections. (A3) Confocal images illustrate pvalb immunoreactivity (Alexa 488) in the cell shown in (*A2*) and a biocytin-filled axon (bcyt, Cy3). Arrows mark colocalized signals. (B, C) AP phase plot defining the firing threshold. (B1) Four superimposed APs evoked as in *A1* in human pvalb cells. (B2) Phase plots showing the first derivative (dV/dt) against Vm (four superimposed curves). (B3) Close-up of the initial AP rise; dotted vertical lines indicate threshold Vm where (dV/dt)

147 reaches 10 mV/ms (horizontal dotted line). (C1) Mouse pvalb cell APs (four superimposed), with

148 corresponding phase plots (C2) and the firing threshold definition (C3). (D) Human pvalb neurons s

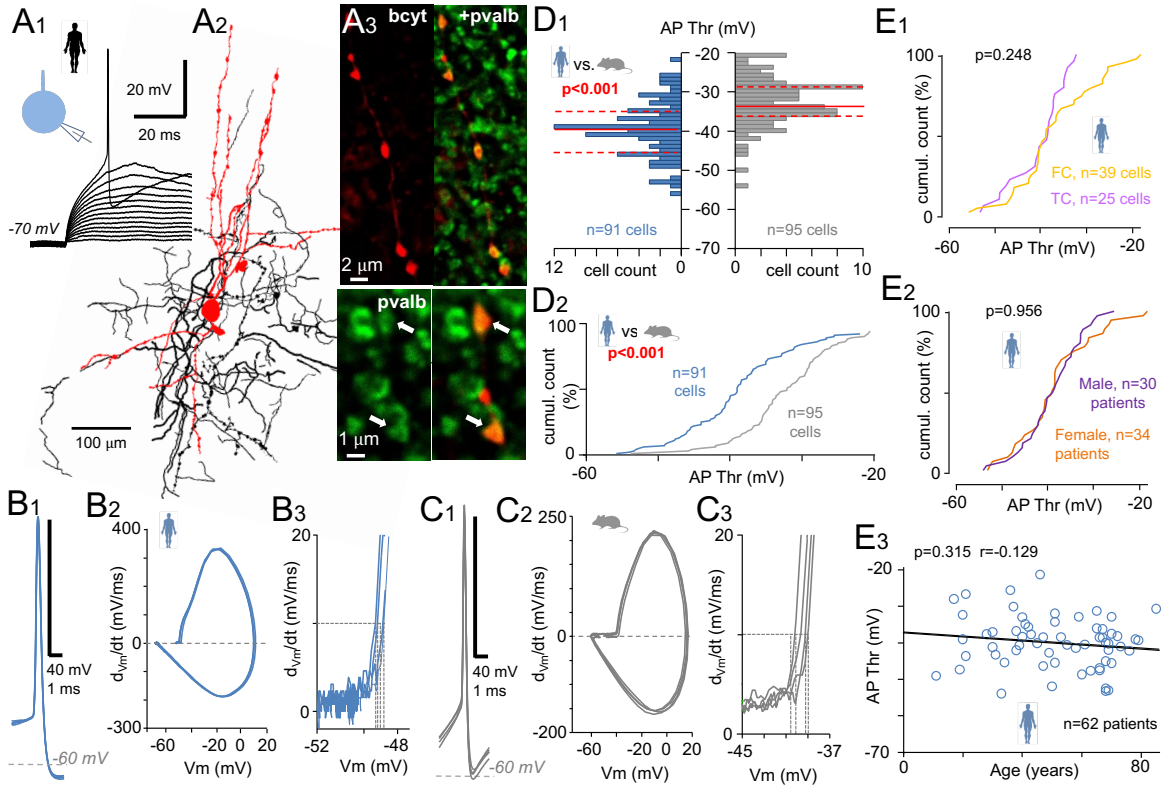

149

150 how a lower AP threshold compared with mouse neurons (Mann–Whitney U test). (D1) AP threshold

151 histograms for human (blue, 91 cells) and mouse (gray, 95 cells) neurons; bin size: 1 mV. Red lines

152 denote median (solid) and quartiles (dotted). (D2) Cumulative histograms of AP threshold in human

153 (blue) and mouse (gray) pvalb cells. (E) In human pvalb neurons, AP threshold was not influenced by

154 (E1) neocortical region [n = 39 cells, frontal cortex (FC); n = 25 cells, temporal cortex (TC)], (E2) sex

155 (threshold calculated as the average per patient; 34 females, 30 males; Mann–Whitney U test), or (E3)

156 age (average per patient; n = 62; Spearman's correlation). Regression line is shown.

157

158 We applied positive Vm steps (square-pulse current steps of increasing amplitude, 500 ms at 1

159 Hz) to cells current-clamped at −70 mV to identify the AP threshold (Fig 1B, C) (defined as

160 the Vm at which the AP initial rise speed reached 10 mV/ms; hereafter, referred to as the firing

161 threshold; Fig 1A1) [31, 36, 44]. Human pvalb neurons had a lower AP threshold [median =

−38.9 mV, interquartile range (IQR) = −42.8 to −34.2, n = 91 cells] compared with mouse neurons (median = −32.5 mV, IQR = −35.9 to −28.3, n = 95 cells, $p < 0.001$; Fig 1D1, 2). They also exhibited lower rheobase current (human cells: 87.34 pA, IQR = 16.8–140.0; mouse cells: 247.65 pA, IQR = 53.95–418.4; $p < 0.001$), a moderately lower AP initial rise slope (human cells: 30.9 ms^{-1}, IQR = 23.82–35.50; mouse cells: 33.2 ms^{-1}, IQR = 28.90–39.01; $p = 0.0011$), and slower AP maximum fall speed (human cells: −122.83 mV/ms, IQR = −165.0 to −82.7; mouse cells: −153.7 mV/ms, IQR = −213.9 to −113.7; $p = 0.001$). AP maximum rise speed was similar across species (human cells: 246.94 mV/ms, IQR = 170.52–335.95; mouse cells: 255.33 mV/ms, 202.10–302.77; $p = 1.00$). Human neurons also had wider AP half-width ($p < 0.001$) and shorter latency to AP generation at rheobase compared with mouse neurons ($p < 0.001$), but no differences were observed in AP peak values ($p = 1.00$) or afterhyperpolarization (AHP) amplitudes ($p = 0.779$). These AP properties and interspecies comparisons are summarized in Table 1 (analyzed via PERMANOVA and Mann–Whitney U test with Bonferroni correction).

Table 1. Features of human and mouse APs from Fig 1.

	Human n = 91			**Mouse n = 95**			
	Median	**1st quartile**	**3rd quartile**	**Median**	**1st quartile**	**3rd quartile**	**P-value**
AP Thr (mV)	−38,9	−42,8	−34,20258	−2,46562	−35,9	−28,3	**<0.001**
Initial rise slope (ms^{-1})	30,9	23,82813	35,5	33,2	28,9	39,01236	**0.037**
AP peak Vm value (mV)	15,6	9,08	25	15,85557	8,17617	23,54049	1
AP half width (ms)	0,496	0,407	0,676	0,36222	0,32	0,416	**<0.001**
AP rheobase (pA)	87,36667	47,53333	140	247,65	142,2	418,4	**<0.001**
AP latency (ms)	19,618	12,6	33,718	50,5	17,94	79,87667	**<0.001**
Spike number by step	3,83333	1,83333	11,75	5	2,5	8	1
AP AHP ampl (mV)	−19,66087	−16,1987	−23,5826	−18,6386	−15,89205	−21,07239	0.7794
Max rise speed (mV/ms)	246,93813	170,51688	335,94748	255,3305	202,10315	320,77388	1
Max fall speed (mV/ms)	−122,83367	−164,99846	−82,73656	−153,73228	−213,90914	−113,678	**0.001**

AP Thr: action potential firing threshold; initial rise slope: maximum slope of the tangent line in the AP phase plot above the threshold (10 mV/ms); AP half-width: measured at 50% of the maximal amplitude

178 from the AP firing threshold to the peak; AP rheobase: amplitude of depolarizing current required to
179 trigger an AP at the AP Thr; AP latency: average time from rheobase current onset to AP onset (defined
180 at AP Thr); spike number: number of APs evoked by the rheobase current step; AP AHP ampl.:
181 amplitude of afterhyperpolarization, measured from AP Thr to AP negative peak; max rise speed:
182 maximum AP rise speed, measured from the AP phase plot; max fall speed: maximum AP fall speed,
183 measured from the AP phase plot). Bolded p-values indicate species differences (PERMANOVA and
184 Mann–Whitney U test with Bonferroni correction).

185

186 We confirmed that AP thresholds in human neurons were similar between frontal (−39.0 mV,
187 IQR = −42.2 to −30.6, n = 39 cells) and temporal cortices (−38.5 mV, IQR = −45.1 to −36.0, n
188 = 25 cells; p = 0.248, Mann–Whitney U test; Fig 1E1). Average AP threshold per subject
189 showed no correlation with demographic factors. Across patients, AP firing thresholds were
190 similar in males (−38.8 mV, IQR = −43.2 to −34.4, n = 30 patients) and females (−39.0 mV,
191 IQR = −44.2 to −33.1, n = 34 patients; p = 0.956, Mann–Whitney U test; Fig 1E2) and unrelated
192 to age (r = −0.129, n = 62 patients; p = 0.315, Spearman's correlation; Fig 1E3). These results
193 show that human pvalb neurons exhibit a lower AP firing threshold in response to somatic
194 excitation compared with mouse pvalb neurons.

195 Low AP threshold is associated with electrically slow somata in 196 pvalb interneurons

197 Compared with mouse pvalb neurons, human pvalb neurons exhibited higher electrical
198 resistance, i.e., input resistance (Rin) in their somata, with no difference in capacitance (Cm).
199 We measured average Rin and Cm using subthreshold Vm steps of +5 to +10 mV (elicited by
200 square-pulse currents at −70 mV; Fig 2A1). Median Rin was 187.9 MΩ (IQR = 103.8–279.8)
201 in human cells (n = 60) versus 125.7 MΩ (IQR = 89.5–167.5) in mouse cells (n = 50; p < 0.001,

Mann–Whitney U test; Fig 2A2). Median Cm in the soma was similar across species (humans: 32.4 pF, IQR = 24.3–53.7, n = 60; mice: 35.1 pF, IQR = 26.3–50.6, n = 50; p = 0.728, Mann–Whitney U test).

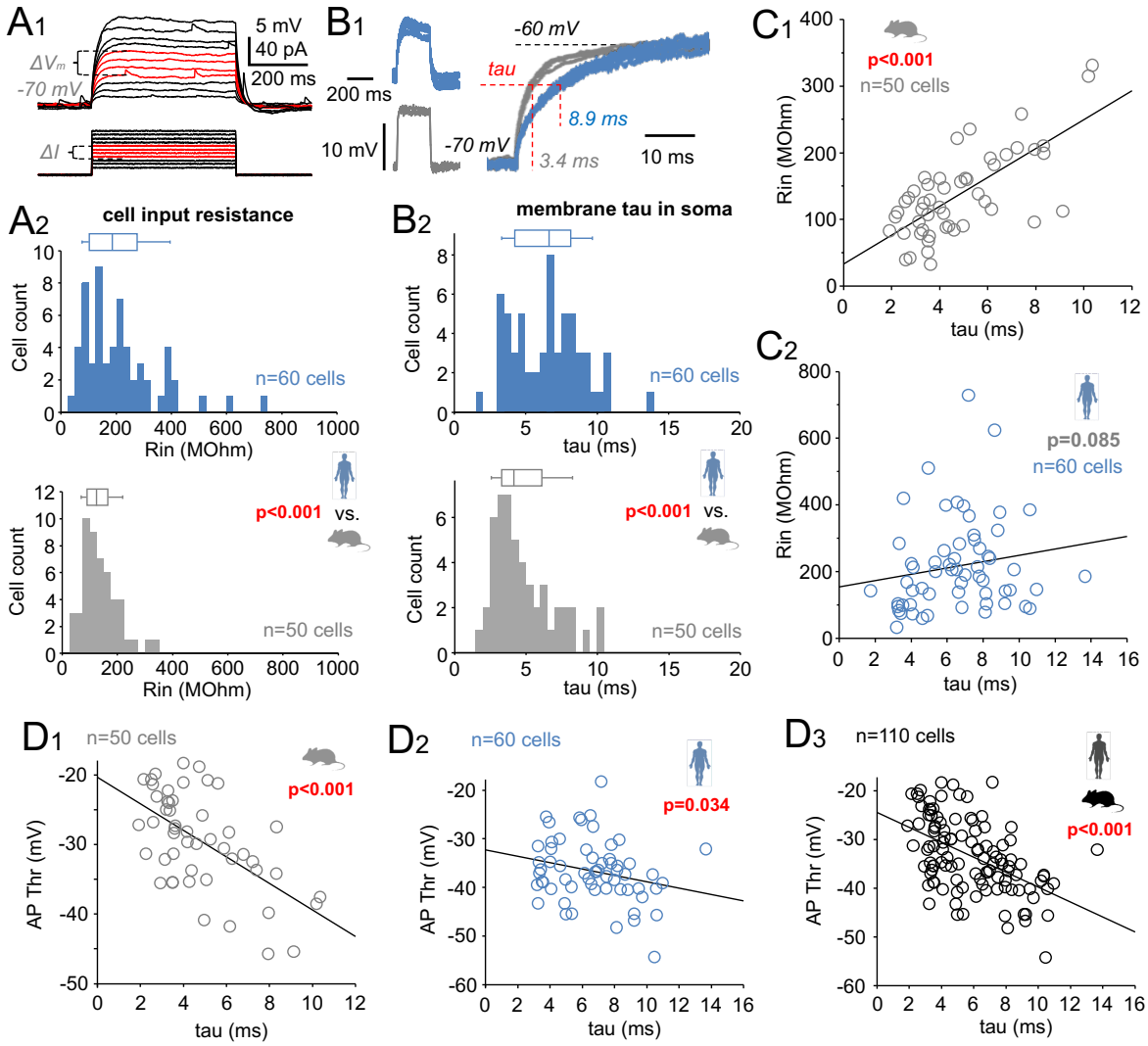

Fig. 2. Low AP firing threshold in pvalb interneurons is associated with an electrically slow soma. (A) Human pvalb cells exhibited higher Rin compared with mouse cells at Vm between −70 mV and the AP threshold. (A1) Cell Rin was measured using positive current steps inducing 5–10-mV subthreshold depolarizations. Voltage shifts (ΔVm) and currents steps (ΔI) used to calculate average Rin are shown in red. (A2) Histograms and box plots show Rin in human (blue) and mouse (gray) pvalb neurons; bin size: 25 MΩ; box plots present the median, quartiles, and 5th and 95th percentiles (Mann–

212 Whitney U test). (B) Tau was longer in human than in mouse pvalb cells for Vm shifts in the soma.
213 (B1) Tau was measured from the ascending phase in +10-mV steps delivered at −70 mV (human: blue;
214 mouse: gray). Left: Four superimposed +10-mV steps in human and mouse cells. Right: Ascending
215 phase shows species differences in tau (human average: 8.9 ms; mouse average: 3.4 ms). (B2)
216 Histograms and box plots illustrate tau differences in human (blue) and mouse (gray) pvalb neurons;
217 bin size: 0.5 ms (Mann–Whitney U test). (C) Soma tau and Rin were strongly associated in mouse (C1)
218 but not human (C2) pvalb neurons (Spearman's correlation). (D) Low AP threshold was linked with
219 slow tau in mouse (D1) and human (D2) pvalb neurons. (D3) Combined data from both species revealed
220 a strong association between slower tau and lower AP threshold (Spearman's correlation).

221

222 The time course of Vm changes (tau), measured from the ascending phase of +10 mV steps,
223 was slower in human pvalb neurons (median tau of the Vm step: 6.65 ms, IQR = 4.22–8.17, n
224 = 60) than in mouse pvalb neurons (median: 4.17 ms, IQR = 3.27–6.12, n = 50; $p < 0.001$,
225 Mann–Whitney U test; Fig 2B1, 2). In mice, tau and Rin showed a significant positive
226 correlation ($r = 0.613$, $n = 50$, $p < 0.001$; Fig 2C1), whereas no such correlation was found in
227 human pvalb neurons ($r = 0.224$, $n = 60$, $p = 0.085$) (Fig 2C2). However, in both species, lower
228 AP thresholds were associated with slower tau (human cells: $r = -0.274$, $n = 60$, $p = 0.034$;
229 mouse cells: $r = -0.535$, $n = 50$, $p < 0.001$; Fig 2D1, 2). Combined data from both species
230 revealed a strong negative correlation between AP threshold and slow tau ($r = -0.514$, $n = 110$;
231 $p < 0.001$, Spearman's correlation; Fig 2D3).

232 Collectively, these results demonstrate that pvalb neurons with slower Vm kinetics to
233 depolarization in the soma tend to have lower AP firing thresholds. This association was
234 particularly strong when analyzing human and mouse pvalb neurons together.

235 # AIS is elongated in human pvalb neurons and exhibits an axonal
236 position associated with AP threshold

237 To explore whether AIS morphology contributes to the lower AP threshold in human
238 pvalb neurons, we visualized the AIS, a primary site of AP initiation, as its length and position
239 can affect AP threshold [45]. We used immunohistochemistry against beta-IV-spectrin, a
240 cytoskeletal protein enriched in the AIS [42, 46, 47], analyzing its immunofluorescence in
241 three-dimensional (3D) confocal microscopy image stacks, with AIS length and distance from
242 the soma quantified using a custom script. All cells were located in layer 2/3 of the neocortex
243 and confirmed as pvalb-positive (Fig 3A1).

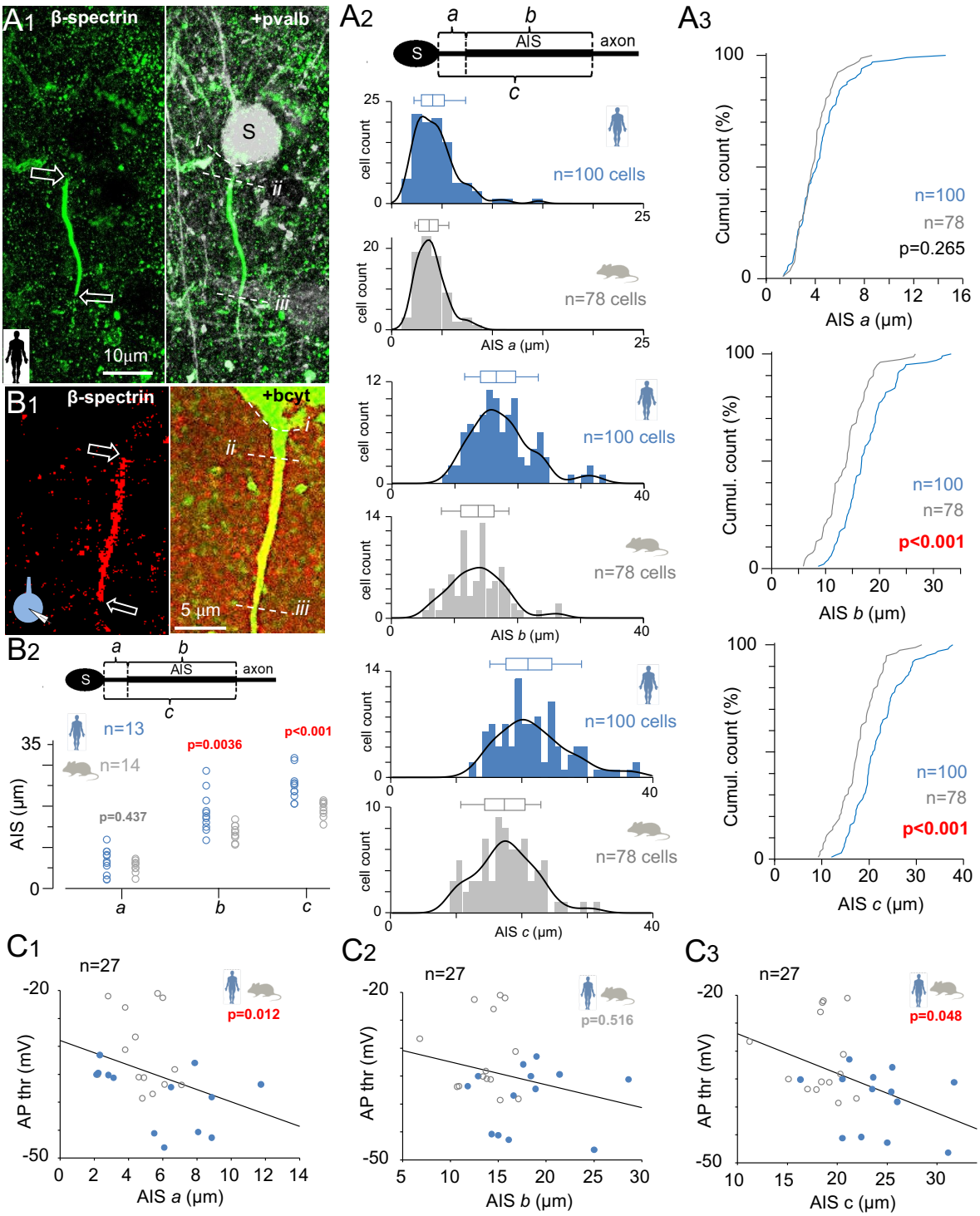

Fig 3. AIS is elongated in human pvalb neurons and axonally located according to AP threshold.

(A) AIS in pvalb neurons was longer in humans than in mice. AIS analysis was performed in triple-immunostained neurons from the human and mouse neocortex. (A1) AIS was measured in 3D fluorescence confocal images of layer 2/3 pvalb-positive neurons. Left: AIS visualized via beta-IV-

249 spectrin immunofluorescence. Arrows indicate AIS initiation and termination sites (Alexa 488) in a
250 collapsed z-stack image of a human pvalb neuron. Right: Merged beta-IV-spectrin and pvalb (Cy5)
251 immunoreactions. Horizontal dotted curves mark (i) the axon from the soma (s) and the proximal (ii)
252 and (iii) distal AIS ends. (A2) Histograms and box plots summarize AIS parameters from the upper
253 schematic: a = distance from the soma to the AIS initiation site, b = AIS length, and c = distance from
254 the soma to the AIS end. Top: AIS initiation distance from the soma did not differ between species.
255 Middle: AIS was longer in human neurons than in mouse neurons. Bottom: AIS termination site was
256 more distal in human neurons than in mouse neurons. Histogram bin: 1 µm, with kernel density; box
257 plots show the median, quartiles, and 5th and 95th percentiles. (A3) Cumulative AIS data show p-values
258 (Student's *t*-test). (B, C) AIS measurements in electrophysiologically investigated pvalb neurons
259 revealed that a low AP threshold is associated with a more distal AIS termination site. (B1) AIS
260 visualized via beta-IV-spectrin immunopositivity (Cy3) in human and mouse cells filled with biocytin
261 (bcyt) and labeled with streptavidin–Alexa 488 conjugates. Immunofluorescence images show AIS
262 features defined in *A1*. (B2) Electrophysiologically studied human pvalb neurons displayed a longer
263 AIS (*b*) with a more distal termination site (*c*) compared with mouse neurons, whereas the AIS start
264 distance (*a*) from the soma did not differ between species (Mann–Whitney U test). Combined AP
265 threshold data from human (blue) and mouse (gray) pvalb neurons revealed associations with AIS
266 initiation site (C1) and termination site (C3) distance from the soma but no association with AIS length
267 (C2) (Spearman's correlation).
268

269 Both human and mouse pvalb neurons exhibited cell-to-cell variation in AIS length and
270 positioning along the axon (Fig 3A2). The median AIS start point was similar between species
271 (humans: 4.12 µm, IQR = 2.95–5.28, n = 100 cells in 17 patients; mice: 3.77 µm, IQR = 2.69–
272 4.68, n = 78 cells in 15 mice; p = 0.265), but the AIS was longer in human cells (median: 16.68
273 µm, IQR = 14.08–19.78) than in mouse cells (median: 13.99 µm, IQR = 11.15–16.55; $p <$
274 0.001). Consequently, the AIS termination site was further from the soma in human neurons

275 (21.01 μm, IQR = 17.60–24.66, n = 100 cells from 17 samples) than in mouse neurons (17.47
276 μm, IQR = 14.41–20.66 μm, n = 78 cells from 15 mice; $p < 0.001$, Mann–Whitney U test; Fig
277 3A2, 3).

278 We also investigated whether these morphological differences relate to the lower AP threshold
279 observed in humans. In electrophysiologically studied and biocytin-filled neurons visualized
280 via streptavidin–fluorophore conjugates, with confirmed immunopositivity for pvalb, we
281 observed the AIS based on beta-IV-spectrin positivity and measured its length and distance
282 from the soma along the axon, comparing these metrics against the AP firing threshold. Of the
283 28 human and 22 mouse cells recorded in the whole-cell clamp, intact somata and full-length
284 AIS were successfully recovered (indicated by beta-IV-spectrin immunofluorescence) in 13
285 human and 14 mouse neurons. In particular, only neurons with biocytin-filled axons extending
286 beyond the distal end of the beta-IV-spectrin–labeled AIS were included, ensuring complete
287 AIS capture for measurement (Fig 3B1). The distance from the AIS's initial point to the soma
288 in human pvalb neurons was 6.10 μm (IQR = 2.55–8.50, n = 13) compared with 4.85 μm (IQR
289 = 3.80–6.03, n = 14) in mouse neurons ($p = 0.437$; Fig 3B2). AIS length was greater in human
290 cells (17.60 μm, IQR = 14.65–20.20 μm) than in mouse cells (14.0 μm, IQR = 12.10–15.33; p
291 = 0.004), and the AIS terminal site was farther from the soma in human neurons (23.60 μm,
292 IQR = 20.85–25.75) than in mouse neurons (18.55 μm, IQR = 17.68–20.38; $p < 0.001$, Mann–
293 Whitney U test). All AIS properties are presented in Fig 3B2. None of the AIS parameters were
294 correlated with the AP threshold in either species. The correlation between AIS proximal
295 distance and AP threshold was 0.536 ($p = 0.054$) in human cells (n = 13) and −0.297 ($p = 0.93$)
296 in mouse cells (n = 14). AIS length was not significantly correlated with AP threshold in
297 humans ($r = 0.203$, $p = 0.493$) or mice ($r = 0.079$, $p = 0.773$), nor was distance from the AIS
298 termination site to the soma correlated with AP threshold in either species (humans: $r = -0.239$,
299 $p = 0.414$; mice: $r = 0.024$, $p = 0.988$, Spearman's correlation). However, when pooling data

300 across species, the AP threshold was significantly correlated with AIS start distance ($r = -0.478$, $p = 0.012$) and AIS termination distance ($r = -0.383$, $p = 0.0485$) but not AIS length
302 ($r = -0.1340$, $p = 0.516$, Spearman's correlation; Fig 3C1–3).

303 These findings indicate that although AIS length and axonal location differ between human
304 and mouse pvalb neurons, only the AIS position shows a consistent relationship with AP
305 threshold when comparing across species. Specifically, greater distal AIS placement is
306 associated with lower AP threshold.

307 Axon diameter does not account for interspecies differences in AP 308 threshold

309 We examined axon diameter in biocytin-filled pvalb interneurons to assess its potential
310 correlation with the AP firing threshold, particularly across species, as axon caliber can
311 influence axon excitability [48]. Axonal diameters were measured using high-magnification
312 fluorescence confocal microscopy images of biocytin-filled neurons at five standardized
313 positions along the axon: two pre-AIS sites and three sites within the AIS (Fig 4A1–3).
314 Reported data represent the mean values per cell for the pre-AIS and within-AIS portions of
315 the axon. No significant differences were observed in axon diameter between human ($n = 12$)
316 and mouse ($n = 14$) pvalb neurons in either in the pre-AIS [1.07 µm (IQR = 0.82–1.19) vs. 0.88
317 µm (IQR = 0.71–1.14); $p = 0.939$] or within-AIS portion [0.83 µm (IQR = 0.70–0.96) vs. 0.69
318 µm (IQR = 0.64–0.74); $p = 0.260$; one-way ANOVA on ranks; Fig 4B]. Additionally, in both
319 AIS portions, axon diameter was not correlated with AP threshold in humans (pre-AIS: $r =$
320 0.245, $p = 0.429$; within-AIS: $r = 0.392$, $p = 0.197$; $n = 12$) or mice (pre-AIS: $r = 0.091$, $p =$
321 0.766; within-AIS: $r = 0.056$, $p = 0.852$; $n = 12$). Pooled data across species also showed no
322 association (pre-AIS: $r = 0.137$, $p = 0.518$; within-AIS: $r = -0.036$, $p = 0.866$, Spearman's

correlation; Fig 4C1, 2). Collectively, these results indicate that axon diameter does not contribute to the observed interspecies differences in AP threshold in pvalb neurons.

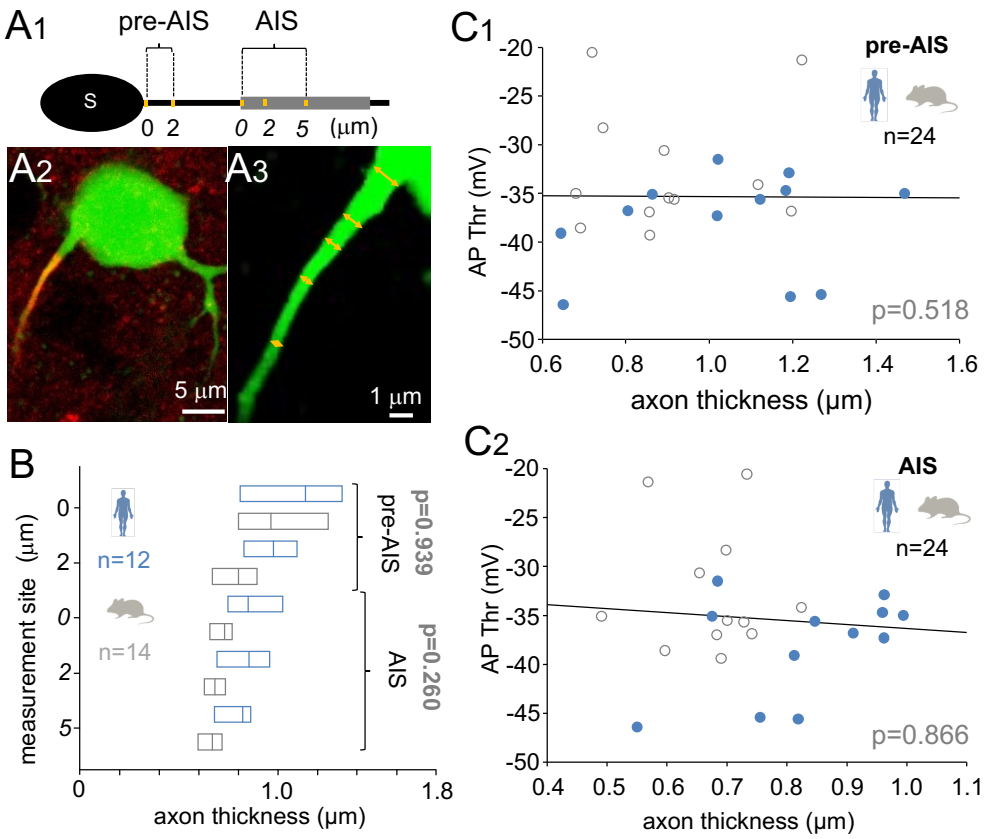

Fig 4. Axon diameter fails to explain interspecies differences in pvalb interneuron AP firing threshold.

(A) Axon cross-diameter was measured in 3D confocal images of biocytin-filled pvalb interneurons. (A1) Schematic showing axon maximum width at five points. "Pre-AIS" measurements were taken at the axon's start (0 µm from the soma) and 2 µm from the soma. "AIS" measurements were taken at the AIS start (shown as *0*) and at *2* and *5* µm from the AIS initiation site. (A2) Collapsed confocal image showing biocytin-filled human pvalb neurons (Alexa 488), with the AIS visualized via beta-IV-spectrin immunoreactivity (Cy3). (A3) Enlarged image of the axon highlighting five measurement sites. (B) Axon thickness was similar between human (blue) and mouse (gray) pvalb neurons. Horizontal bars indicate medians and quartiles. (C) Axon diameter was not correlated with AP threshold in either the

336 pre-AIS region (C1) or the AIS (C2). Data from both species were pooled (one-way ANOVA on ranks
337 with Dunn's pairwise *post hoc* test).
338

339 Nav1.6 channels are similarly distributed in the AIS of human and 340 mouse pvalb neurons

341 We examined immunoreactivity for the low-voltage-gated sodium channel Nav1.6 in
342 the soma and axon of pvalb neurons (Fig 5A–H), as Nav1.6 density and spatial distribution in
343 the AIS can regulate AP threshold [49, 50]. Nav1.6 may concentrate at the AIS's distal end to
344 lower the AP firing threshold [48, 49, 51, 52], or it may be evenly distributed. In layer 2/3 of
345 the human and mouse neocortex, we assessed Nav1.6 immunofluorescence (Fig 5A1, 2)
346 intensity using confocal microscopy images of the soma (Fig 5B1, 2) and 3D image stacks
347 along the axon (Fig 5C1, 2) to evaluate species-specific differences in Nav1.6 channel
348 distribution. In individual human cells (n = 21; Fig 5D1) and mouse cells (n = 26; Fig 5D2),
349 24 radial lines were drawn from within the soma to the extracellular space to measure Nav1.6
350 (Cy3) and pvalb (Cy5) immunofluorescence. Because pvalb is intracellular, its onset along
351 each line defined the extracellular membrane site (Fig 5D1, 2). We also measured
352 immunofluorescence intensity for Nav1.6, pvalb, and beta-IV-spectrin in the same cells along
353 the axon, annotated in 3D image stacks, from the soma to beyond the AIS termination site (Fig
354 5E1, 2).

355 **Fig 5. AIS displays robust and uniform immunofluorescence for Nav1.6 channels in human and**
356 **mouse pvalb neurons.**

357 (A) Triple immunofluorescence for pvalb (Cy5), beta-IV-spectrin (Alexa 488), and Nav1.6 (Cy3)
358 revealed sodium channel localization in the AIS of human (A1) and mouse (A2) pvalb neurons. Arrows

359 mark AIS initiation and termination sites; s indicates the soma. Images are collapsed z-stacks from layer
360 2/3 of the neocortex. (B) Nav1.6 immunofluorescence in the somatic cytoplasm and membrane was
361 analyzed alongside pvalb in human (B1) and mouse (B2) cells. Immunofluorescence intensity was
362 measured using a 24-line radial pattern (yellow lines) extending from the extracellular space to the soma
363 center. (C) Nav1.6 intensity was measured along the axon from the soma (s) past the AIS termination
364 site in 3D confocal images. Measurement lines in human (C1) and mouse (C2) pvalb neurons overlie
365 beta-IV-spectrin–defined AIS (masked in the images by the lines). Images are collapsed from z-stacks.
366 (D) Immunofluorescence intensity [ordinate, arbitrary unit (a.u.)] was measured for pvalb (top, black
367 line) and Nav1.6 (bottom, red line) along radial lines spanning the extracellular space (negative abscissa
368 values) to the soma (positive values). Vertical dashed line denotes the membrane location (0-point),
369 defined as ±0.5 µm from the first pvalb signal. (D1) Left: Mean fluorescence intensity (F, a.u.) across
370 24 radial lines in one human cell, spanning −3 to +1.5 µm. Schematic illustrates measurement geometry.
371 Right: Medians and quartiles of intensity values minus the extracellular reference ($F-F_{ex.c}$) in 21 human
372 cells. (D2) Identical measurements as in *D1* for one mouse cell (left) and 26 mouse cells (medians and
373 quartiles; right). (E) Fluorescence intensity along 3D pixel lines for pvalb (black), beta-IV-spectrin
374 (green), and Nav1.6 (red). (E1) Left: Measurement in one human neuron (a.u.); 0 on abscissa = axon
375 origin. Upper schematic illustrates the measurement line along the axon. Right: Medians and quartiles
376 of referenced intensity values ($F-F_{ex.c}$) in 21 human cells. Upper schematic indicates the defined AIS
377 (determined via beta-IV-spectrin immunofluorescence) and pre-AIS and post-AIS axonal regions. AIS
378 length (green background) was divided into 10 bins per cell. Statistical analysis showed no difference
379 in Nav1.6 intensity between proximal and distal AIS halves (Mann–Whitney U test). (E2) Same
380 measurements shown in *E1* for one mouse cell (left) and 26 mouse cells (right; medians and quartiles).
381 (F, G) Summary of line analyses in human and mouse pvalb neurons; medians and quartiles of $F-F_{ex.c}$
382 across five cellular domains showed strong Nav1.6 immunoreactivity in the AIS. (H) $F-F_{ex.c}$ values
383 across domains did not differ between human (blue) and mouse (gray) pvalb cells (PERMANOVA with
384 Bonferroni *post hoc* test).
385

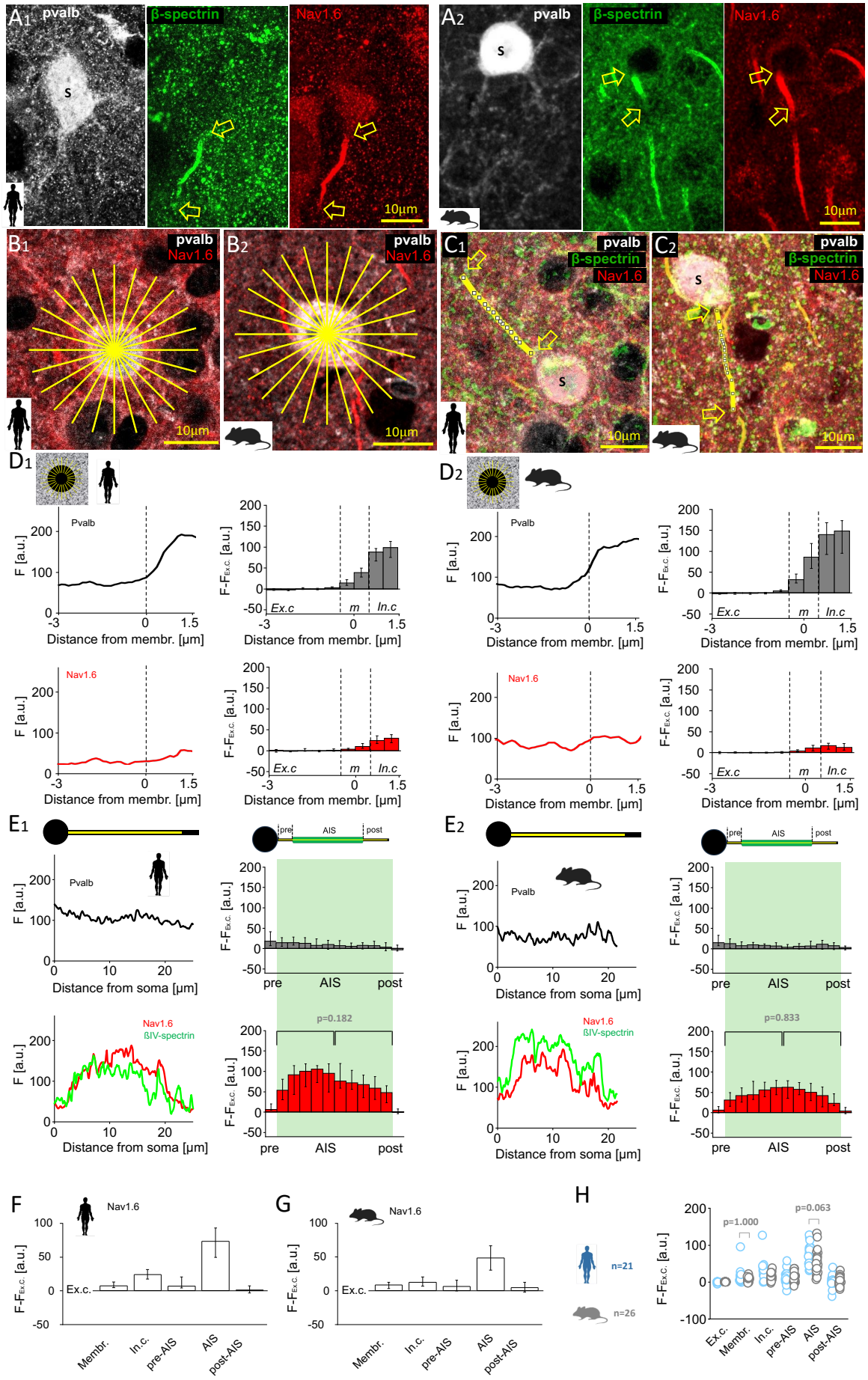
A1
pvalb
β-spectrin
Nav1.6
s
10µm
A2
B1
B2
C1
C2
D1
D2
Pvalb
Nav1.6
F [a.u.]
Distance from membr. [µm]
F-FEx.c. [a.u.]
Ex.c
m
In.c
E1
E2
pre
AIS
post
Distance from soma [µm]
ßIV-spectrin
p=0.182
p=0.833
F
G
H
Ex.c.
Membr.
In.c.
pre-AIS
post-AIS
n=21
n=26
p=1.000
p=0.063

386

387 Reference-corrected Nav1.6 immunofluorescence ($F–F_{ex.c.}$, defined as the fluorescence
388 intensity with the extracellular average subtracted from other radial or axon pixels) was similar
389 across species in the soma membrane (humans: 7.06, IQR 4.72–15.12, n =21; mice: 8.52, IQR
390 = 3.30–12.50, n = 26; p = 1.00) and the cytoplasm (humans: 23.66, IQR = 16.37–31.64, n =
391 21; mice: 12.39, IQR = 5.88–20.25, n = 26; p = 0.067).

392 Nav1.6 immunofluorescence was similarly weak in human and mouse pre-AIS axons (humans:
393 6.55, IQR = 4.03–20.69, n =21; mice: 6.25, IQR = −0.87–16.24, n =26; p = 1.00) and post-AIS
394 regions (humans: 0.95, IQR = −3.41 to 7.56; mice: 4.59, IQR = −2.49 to 13.13; p = 1.00).
395 Nav1.6 intensity was strong in the AIS but not significantly different between humans (73.18,
396 IQR = 49.32–94.05) and mice (48.40, IQR = 28.84–67.81; p = 0.063, PERMANOVA and
397 Mann–Whitney U test with Bonferroni correction; Fig 5E1, 2). In both species, Nav1.6
398 immunofluorescence was uniformly distributed within the AIS, with no difference between the
399 first and second halves (humans: p = 0.182; mice: p = 0.833, Mann–Whitney U test; Fig 5E1,
400 2). Nav1.6 $F–F_{ex.c}$ values are shown in Fig 5F for humans and Fig 5G for mice, with is no
401 species differences observed (Fig 5H).

402 Human pvalb neurons exhibit low Kv1 channel levels in the AIS
403 relative to mouse neurons

404 We investigated the immunofluorescence of Kv1.1 and Kv1.2 potassium channels, key
405 inhibitory mechanisms modulating AP threshold in the AIS [53, 54]. Kv1 channels are
406 clustered in the AIS and soma of rodent pvalb neurons [55], where they increase the AP firing
407 threshold [53, 56] (hereafter, Kv1 channels are referred to as inhibitory channels). First, we
408 analyzed Kv1.1 immunofluorescence in the soma and AIS of human (Fig 6A1) and mouse (Fig
409 6A2) pvalb neurons using triple immunolabeling. Representative cells and analysis are shown

410 in Fig 6B and C, including those in the soma (Fig 6B1, 2) and along the axon (Fig 6C1, 2). $F-$
411 $F_{ex.c.}$ analysis showed absent Kv1.1 signal at the human soma membrane (−1.23, IQR = −4.77
412 to 5.25, n = 31) as well as its presence in mice (5.42, IQR = 0.62–10.58, n = 31; p = 0.041).
413 Kv1.1 signal in the cytoplasm was weak in both species and did not differ significantly (p =
414 0.817; Fig 6D1, 2).

415 **Fig 6. AIS is deficient in Kv1.1 potassium channels in humans compared with mice.**

416 (A) Immunofluorescence staining revealed a species-specific difference in Kv1.1 expression in the AIS
417 of pvalb neurons. (A1) Triple labeling for beta-IV-spectrin (Alexa 488), Kv1.1 (Cy3), and pvalb (Cy5)
418 in the human neocortex layer 2/3. Open arrows denote the AIS visualized using beta-IV-spectrin in a
419 pvalb+ neuron; solid arrows mark the AIS of a pvalb− neuron; s denotes the pvalb+ soma. The pvalb+
420 neuron lacked a Kv1.1 signal, whereas the pvalb− AIS exhibited robust Kv1.1 labeling. (A2) Same
421 triple labeling shown in *A1* in the mouse cortex; both pvalb+ (open arrows) and pvalb− (solid arrows)
422 neurons showed robust AIS Kv1.1 expression. (B) Kv1.1 fluorescence intensity in somatic membranes
423 analyzed with pvalb labeling in human (B1) and mouse (B2) neurons. Yellow radial lines indicate the
424 24-line measurement pattern. (C) Axonal Kv1.1 intensity was measured from the soma (s) in 3D
425 confocal images in human (C1) and mouse (C2) neurons. Measurement lines are shown above the beta-
426 IV-spectrin–labeled AIS in collapsed z-stacks. (D) Fluorescence intensity for pvalb (top, black line)
427 and Kv1.1 (bottom, red line) along radial lines in the soma. Vertical dashed line marks pvalb signal
428 onset (0-point). (D1) Left: Mean intensity (F, a.u.) across 24 radial lines in one human cell, spanning
429 −3 to +1.5 μm. Schematic shows radial lines. Right: Medians and quartiles of $F-F_{ex.c}$ in 31 human cells
430 for pvalb (gray) and Kv1.1. (red). (D2) Same measurements as in *D1* for one mouse cell (left) and 31
431 mouse cells (right; medians and quartiles). (E) Line analysis of axons for pvalb (black), beta-IV-spectrin
432 (green), and Kv1.1 (red). (E1) Left: Intensity profile of one human cell, as illustrated in upper schematic
433 (0 = the axon origin). Right: Medians and quartiles of $F-F_{ex.}$ intensity values in 31 human cells. Upper
434 schematic shows AIS defined by beta-IV-spectrin labeling. AIS length (green background) was divided
435 into 10 bins per cell. Statistical analysis revealed that Kv1.1 intensity does not differ between the

436 proximal and distal AIS halves (Mann-Whitney U test). (E2) Identical measurements described in *E1*
437 for one mouse neuron (left) and 31 mouse neurons (right; medians and quartiles). Statistical analysis
438 indicated that Kv1.1. is evenly distributed along the AIS (Mann-Whitney U test). (F, G) Summary of
439 line analyses in human and mouse pvalb neurons; medians and quartiles of $F-F_{ex.c}$ for Kv1.1 across
440 cellular domains. (H) $F-F_{ex.c}$ values in human (blue) and mouse (gray) pvalb cells across cellular
441 domains: mouse cells showed stronger Kv1.1 signals in the somatic membrane and AIS compared with
442 human cells (PERMANOVA test with Bonferroni *post hoc* test).
443

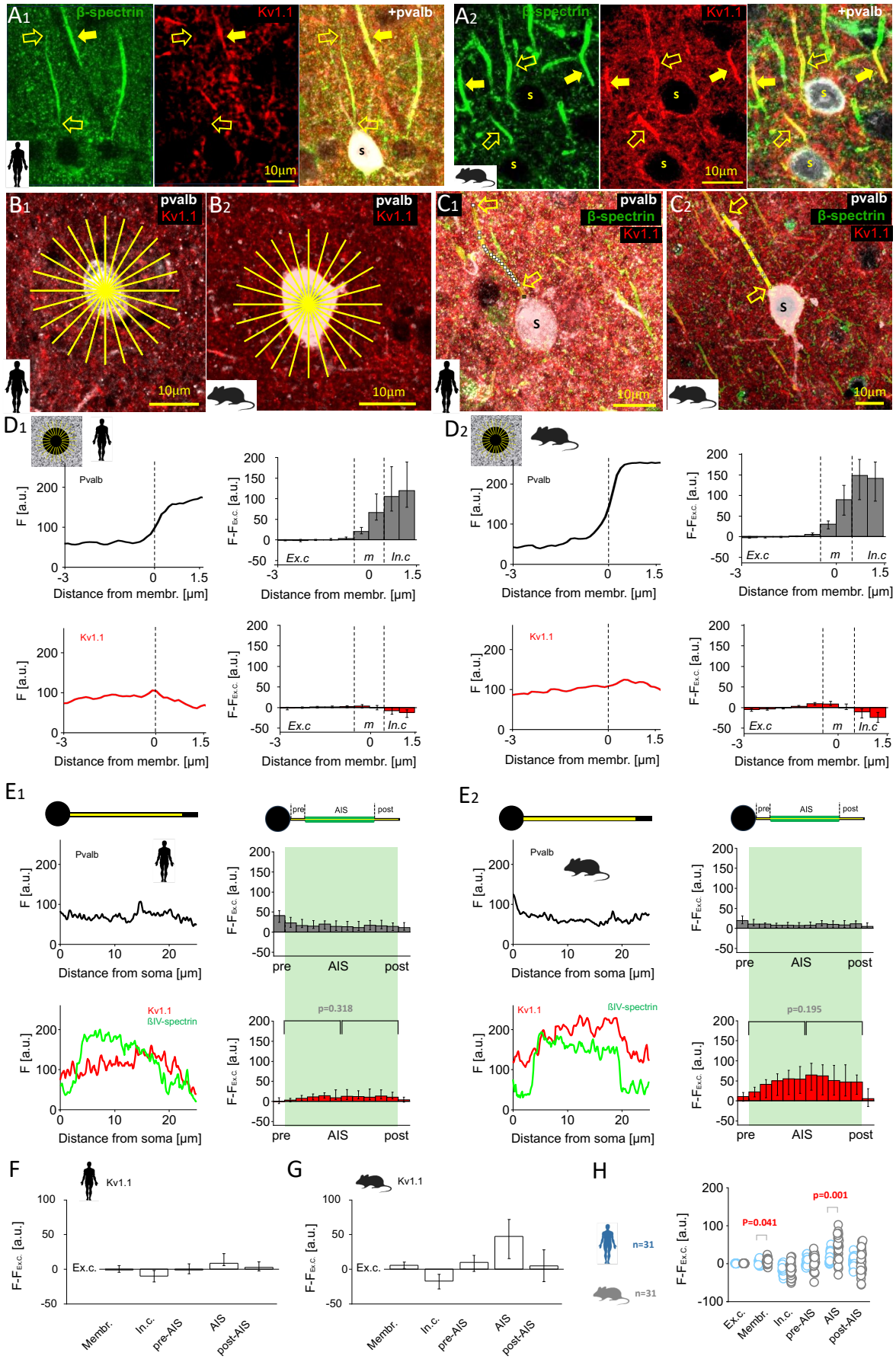
A1
β-spectrin
Kv1.1
+pvalb
10µm
A2
B1
pvalb
Kv1.1
B2
C1
β-spectrin
C2
D1
D2
Pvalb
F [a.u.]
Distance from membr. [µm]
F-FEx.c [a.u.]
Ex.c
m
In.c
E1
E2
Distance from soma [µm]
pre
AIS
post
p=0.318
p=0.195
ßIV-spectrin
F
G
H
Membr.
In.c.
pre-AIS
post-AIS
Ex.c.
n=31
P=0.041
p=0.001

444

445 Axonal analysis showed robust Kv1.1 signal in the AIS of mouse cells (47.56, IQR = 13.98–
446 74.95, n = 31), consistent with previous reports [53]. In contrast, human AIS Kv1.1 signal was
447 low or absent (8.54, IQR 5.00–24.43), despite strong signal in nearby pvalb-negative neurons
448 (Fig 6A1). AIS $F–F_{ex.c.}$ differed between species (p = 0.001; Fig 6E1, 2). Pre-AIS (humans:
449 −1.06, IQR = −6.71 to 8.77; mice: 9.56, IQR = −5.49 to 20.32; p = 0.287) and post-AIS
450 (humans: 2.55, IQR = −3.26 to 10.88; mice: 4.58, IQR = −17.97 to 29.20; p = 1.00) regions
451 showed no significant differences (PERMANOVA and Mann–Whitney U test with Bonferroni
452 correction.). Kv1.1 intensity showed no difference between AIS halves (humans: p = 0.318;
453 mice: p = 0.195, Mann–Whitney U test; Fig 6E1, 2). Kv1.1 $F–F_{ex.c.}$ intensity values for each
454 domain are summarized in Fig 6F and G, and species comparisons are shown in Fig 6H.

455 We also analyzed Kv1.2 immunofluorescence (Fig 7A1, 2), comparing $F–F_{ex.c.}$ in the soma
456 (Fig 7B1, 2) and AIS (Fig 7C1, 2) of human and mouse pvalb neurons [57]. A low but
457 moderately higher Kv1.2 signal was observed at the human soma membrane (5.74, IQR = 2.08–
458 10.42, n = 60) compared with the mouse membrane (3.42, IQR = −2.66 to 5.30, n = 33; p =
459 0.013; Fig 7D1, 2). Cytoplasmic signal was also higher in humans (4.47, IQR = −3.73 to 16.39)
460 than in mice (−6.59, IQR = −12.07 to 4.16; p = 0.002).

461 **Fig 7. Kv1.2 potassium channel expression is low in the AIS of human and mouse pvalb neurons.**

462 (A) Triple immunofluorescence for beta-IV-spectrin (Alexa 488), Kv1.2 (Cy3), and pvalb (Cy5)
463 revealed weak Kv1.2 immunoreactivity in the AIS of human (A1) and mouse (A2) pvalb neurons. Open
464 arrows indicate AIS identified via beta-IV-spectrin in a pvalb+ neurons, which show negligible Kv1.2
465 signal; solid arrow denotes a Kv1.2-positive dendrite and somatic membrane of another neuron; s marks
466 the pvalb+ soma. (B) Radial intensity measurements of Kv1.2 and pvalb in human (B1) and mouse (B2)
467 somata using 24-line radial patterns (yellow lines). (C) Line measurements of Kv1.2 intensity along the
468 axon from the soma (s) in human (C1) and mouse (C2) pvalb neurons. Images are collapsed z-stacks;
469 line measurement is shown over the axon. (D) Immunofluorescence intensity profiles for pvalb (top,

470 black line) and Kv1.2 (bottom, red line) along the radial lines in the soma. (D1) Left: Mean fluorescence
471 intensity (F, a.u.) in 24 pooled lines from one human cell, spanning −3 to +1.5 µm from the 0-point.
472 Right: Medians and quartiles of $F-F_{ex.c}$ values for pvalb (gray) and Kv1.2. (red) in 60 human cells.
473 (D2) Identical measurements as in *D1* for one mouse cell (left) and 33 mouse cells (right; medians and
474 quartiles). (E) Axonal line analysis for pvalb (black), beta-IV-spectrin (green), and Kv1.2 (red). E1)
475 Left: Line intensity values along the axon in one human cell (illustrated in the upper schematic), with 0
476 denoting the axon origin. Right: Median and quartiles of $F-F_{ex.}$ values across 60 human cells. AIS
477 length (green background) was divided into 10 bins. Statistical analysis showed similarly negligible
478 Kv1.2 intensity in the proximal and distal AIS halves (Mann-Whitney U test). (E2) Identical
479 measurement as in *E1* for one mouse neuron (left) and 33 mouse neurons (right; medians and quartiles),
480 showing uniformly low Kv1.2 signal across the AIS (Mann-Whitney U test). (F, G) Summary of line
481 analyses in human and mouse pvalb cells; medians and quartiles of $F-F_{ex.c}$ values across cellular
482 domains. (H) $F-F_{ex.c}$ values in human (blue) and mouse (gray) pvalb cells: human cells showed stronger
483 Kv1.2 signals in the somatic membrane compared with mouse cells (PERMANOVA test with
484 Bonferroni *post hoc* test).
485

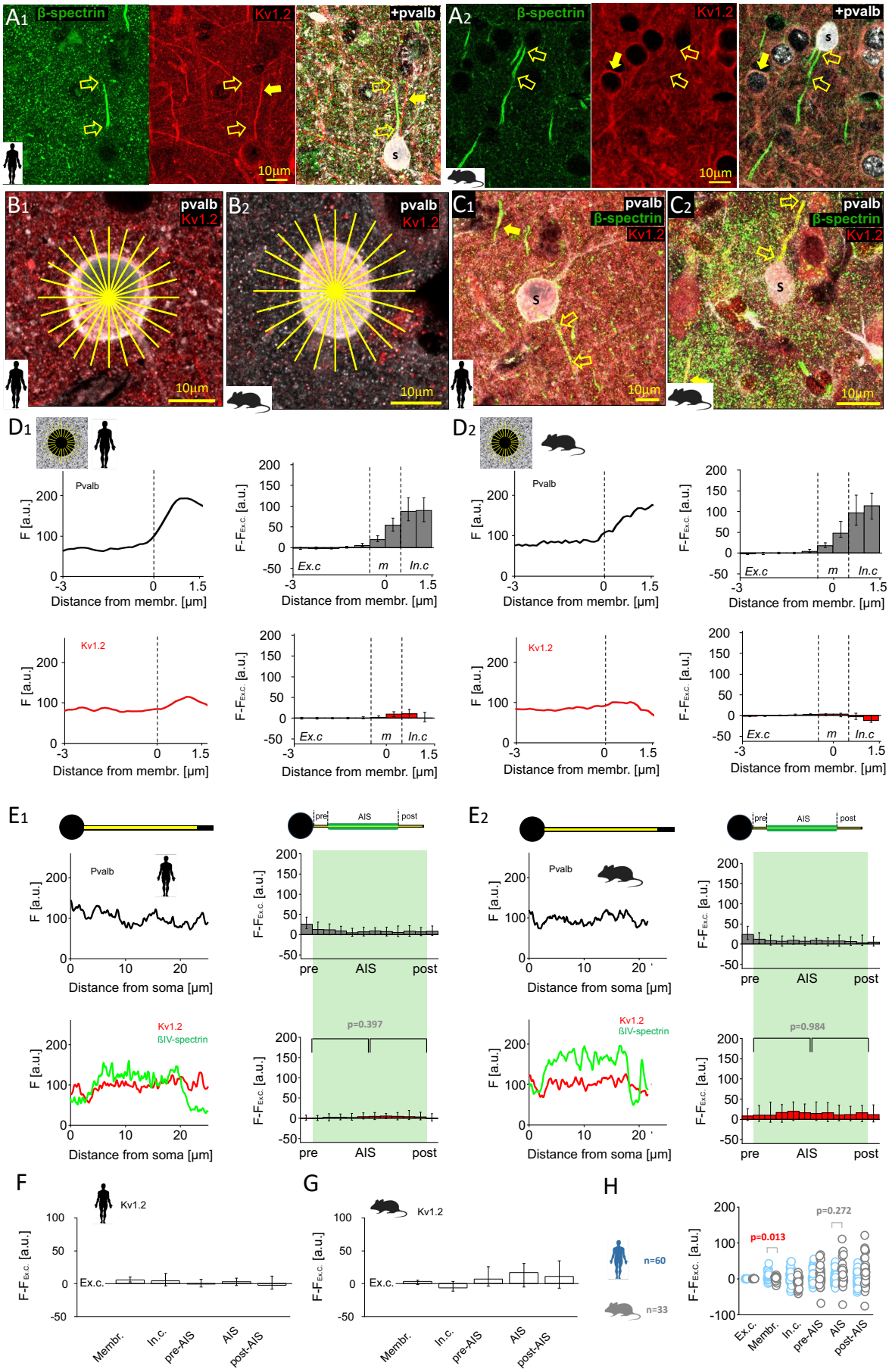
A1
β-spectrin
Kv1.2
+pvalb
10µm
A2
β-spectrin
Kv1.2
+pvalb
10µm
B1
pvalb
Kv1.2
10µm
B2
pvalb
Kv1.2
10µm
C1
pvalb
β-spectrin
Kv1.2
10µm
C2
pvalb
β-spectrin
Kv1.2
10µm
D1
D2
Pvalb
Kv1.2
F [a.u.]
F-FEx.C. [a.u.]
Distance from membr. [µm]
Ex.c
m
In.c
E1
E2
pre
AIS
post
Distance from soma [µm]
Kv1.2
ßIV-spectrin
p=0.397
p=0.984
F
G
H
Kv1.2
Ex.c.
Membr.
In.c.
pre-AIS
AIS
post-AIS
n=60
n=33
p=0.013
p=0.272

486

487 In the AIS, no difference in Kv1.2 $F–F_{ex.c.}$ was detected between human (2.95, IQR = −3.23 to
488 9.05, n = 60) and mouse (17.04, IQR = −5.30 to 31.76, n = 30) cells (p = 0.272; Fig 7E1, 2),
489 nor in pre-AIS (p = 0.478) or post-AIS (p = 0.187) sites (PERMANOVA and Mann–Whitney
490 U test with Bonferroni correction). Kv1.2 immunofluorescence intensity showed no difference
491 between AIS halves (humans: p = 0.397; mice: p = 0.984, Mann–Whitney U test; Fig 7E1, 2).
492 Kv1.2 data are summarized in Fig 7F, G and H.

493 Pvalb neurons in humans lack *KCNA1* mRNA encoding Kv1.1 but 494 possess *KCNA2* mRNA encoding Kv1.2

495 We used patch-sequencing to measure the mRNA levels of low-threshold ion channels
496 that regulate the AP firing threshold, namely Kv1.1 and Kv1.2 [44, 51, 53-55, 58], in
497 electrophysiologically studied fast-spiking pvalb neurons in human and mouse neocortex layer
498 2/3. Whole-cell recordings were followed by nucleus extraction and transcriptomic analysis
499 [59, 60]. We detected mRNA for 6,784 genes (IQR = 4872–7399) in humans (n = 21) and
500 3,617 genes (IQR = 3173–4305) in mice (n = 16; Fig 8A). Transcriptomes were uploaded to
501 the Allen Institute neuron type identification server, which employs an algorithm categorizing
502 neocortex layer 2/3 neuron types by gene expression (https://knowledge.brain-
503 map.org/mapmycells/process/), enabling identification of pvalb neurons, even in cells with
504 undetectable *PVALB* mRNA expression. Using this method, we identified 21 and 16 human
505 and mouse pvalb neurons, respectively. These cells were analyzed for expression of *KCNA1*,
506 *KCNA2*, *KCNC1*, *KCNC2*, *KCND1*, *KCNQ1*, *KCNQ2*, *KCNQ3*, *KCNQ4*, *KCNQ5*, *KCNK2*,
507 *KCNK4*, and *KCK10*, i.e., genes encoding major potassium channels in axons that regulate AP
508 threshold [54, 55]. Additionally, we analyzed *SCN8A* expression and that of the housekeeping
509 genes *ACTB*, *GAPDH*, and *SLC8A1* (Fig 8A).

510 **Fig. 8. Human pvalb neurons lack *KCNA1* mRNA and express low *KCNA2* mRNA levels.**

511 (A) Patch-sequencing analysis (illustrated in the upper schematic) revealed that human pvalb neurons
512 do not express *KCNA1*, in contrast to its expression in mouse cells. (A1) Heatmap showing transcript
513 levels (TPM) of genes encoding low-threshold potassium channels in individual human (n = 21) and
514 mouse (n = 16) pvalb neurons, as well as the housekeeping genes *GAPDH* and *ACTB*. *KCNA1*
515 expression differed quantitatively (TPM values) and categorically (positive or negative gene
516 expression) in human and mouse cells. Expression of *KCNA2*, *KCNC1*, *KCNC2*, *KCNK2*, *KCNK4*, and
517 *KCNK10* was observed in both species (*61*), whereas *KCND1* expression was nearly absent in both
518 (*62*). Human and mouse cells expressed similar levels of *KCNQ1*, *KCNQ2*, and *KCQN4*, whereas
519 *KCNQ3* and *KCNQ5* expression levels were higher in humans. Additionally, *SCN8A* (encoding Nav1.6
520 channels) and *SLC6A1* (encoding GABA transporter type-1) were highly expressed in both species.
521 Significant differences in TPM values are marked in red (genes, ordinate). Bottom of the heatmap shows
522 the pvalb cell subtype classification based on Allen Institute transcriptomic data. (B) Allen Institute
523 database analysis of layer 2/3 pvalb neuron subtypes in the human and mouse neocortex confirmed
524 *KCNA1* mRNA deficiency in human cells. Heatmap shows average TPM values (scale on the right)
525 across seven human and eight mouse pvalb neuron subtypes (abscissa). *KCNA1* mRNA was absent in
526 all human subtypes but robustly expressed in mouse cells. Statistical analyses (one-way MANOVA
527 with Bonferroni *post hoc* test and chi-squared test with Benjamini–Hochberg adjustment) confirmed
528 significant differences in both expression level and frequency ($p = 0.0011$ and $p < 0.001$, respectively).
529 *KCNQ3* and *KCNQ5* expression levels were higher in humans. Significant differences in TPM values
530 are marked in red (genes, ordinate). Abscissa shows pvalb cell subtype names.

531

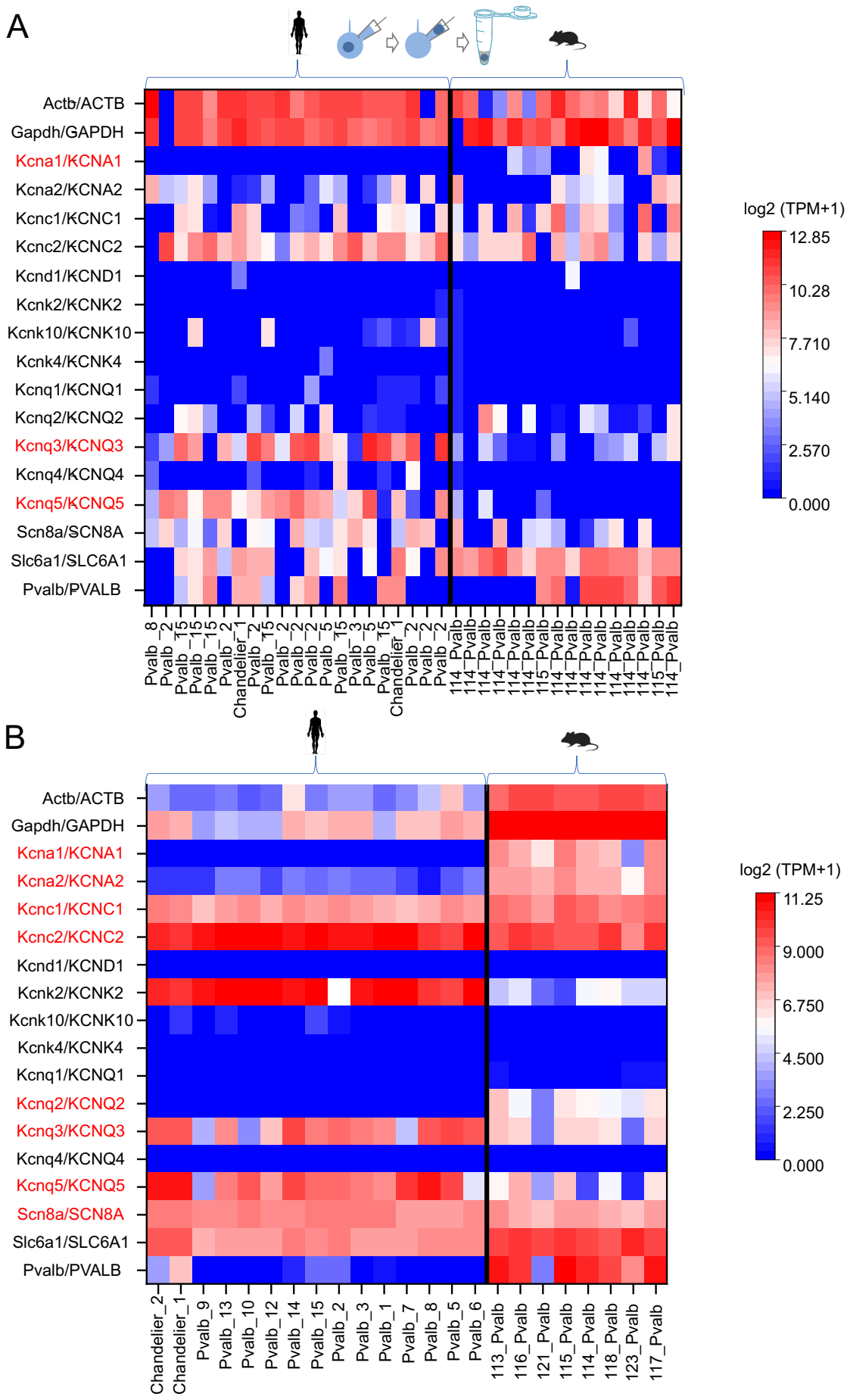
A
Actb/ACTB
Gapdh/GAPDH
Kcna1/KCNA1
Kcna2/KCNA2
Kcnc1/KCNC1
Kcnc2/KCNC2
Kcnd1/KCND1
Kcnk2/KCNK2
Kcnk10/KCNK10
Kcnk4/KCNK4
Kcnq1/KCNQ1
Kcnq2/KCNQ2
Kcnq3/KCNQ3
Kcnq4/KCNQ4
Kcnq5/KCNQ5
Scn8a/SCN8A
Slc6a1/SLC6A1
Pvalb/PVALB
log2 (TPM+1)
12.85
10.28
7.710
5.140
2.570
0.000
B
Actb/ACTB
Gapdh/GAPDH
Kcna1/KCNA1
Kcna2/KCNA2
Kcnc1/KCNC1
Kcnc2/KCNC2
Kcnd1/KCND1
Kcnk2/KCNK2
Kcnk10/KCNK10
Kcnk4/KCNK4
Kcnq1/KCNQ1
Kcnq2/KCNQ2
Kcnq3/KCNQ3
Kcnq4/KCNQ4
Kcnq5/KCNQ5
Scn8a/SCN8A
Slc6a1/SLC6A1
Pvalb/PVALB
Chandelier_2
Chandelier_1
Pvalb_9
Pvalb_13
Pvalb_10
Pvalb_12
Pvalb_14
Pvalb_15
Pvalb_2
Pvalb_3
Pvalb_1
Pvalb_7
Pvalb_8
Pvalb_5
Pvalb_6
113_Pvalb
116_Pvalb
121_Pvalb
115_Pvalb
114_Pvalb
118_Pvalb
123_Pvalb
117_Pvalb
log2 (TPM+1)
11.25
9.000
6.750
4.500
2.250
0.000

532

533 All 21 human pvalb neurons lacked detectable *KCNA1* mRNA expression, whereas 7 of 16
534 mouse neurons showed robust expression. The mRNA level heatmap in Fig 8A shows the gene
535 expression (transcripts per million [(TPM]) of individual pvalb neurons in humans and mice.
536 Comparing *KCNA1* mRNA expression between human (n = 21) and mouse cells (n = 16)
537 revealed a significant difference (p = 0.0016, one-way MANOVA with a *post hoc* Bonferroni
538 test). Furthermore, categorical comparisons (positive or negative mRNA expression)
539 confirmed that *KCNA1* expression differed significantly between species (p < 0.001, chi-
540 squared test following Benjamini–Hochberg adjustment at the 5% significance level; Fig 8A).
541 Both species displayed *KCNA2* mRNA expression without any species-specific difference (p
542 = 0.970). We also tested whether pooled mRNA levels (TPM) of *KCNA1* and *KCNA2* were
543 associated with AP threshold in patch-sequenced neurons. No association was observed for
544 either gene in humans (r = 0.041, n = 20, p = 0.861) or mice (r = 0.236, n = 15, p = 0.388).
545 When neurons from both species were pooled, the results remained nonsignificant (r = 0.175,
546 n = 35; p = 0.312, Spearman's correlation test).

547 Both species exhibited similarly strong *KCNC1* and *KCNC2* mRNA expression, which
548 respectively encode the Kv.3.1 and Kv3.2 channels characteristics of pvalb interneurons [43,
549 61]. They also showed equally low or undetectable expression of *KCND1* encoding Kv4.1
550 potassium channels [62]. No species differences were observed in *KCNK2*, *KCNK4*, or
551 *KCNK10* mRNA levels, and *KCNQ1*, *KCNQ2*, and *KCNQ4* mRNAs were similarly expressed
552 between species. However, human neurons displayed significantly higher mRNA levels of
553 *KCNQ3* (p < 0.001) and *KCNQ5* (p < 0.001). Both human and mouse pvalb cells strongly
554 expressed *SCN8A* mRNA, encoding Nav1.6 sodium channels. Additionally, all cells expressed
555 high levels of *ACTB* and *GAPDH*. Notably, mRNA expression of *SLC6A1*, which encodes
556 GABA transporter 1, was significantly lower in human neurons than in mouse neurons (p =
557 0.002). *PVALB* mRNA expression was undetectable in 10 of 21 human neurons and 6 of 16

558 mouse neurons, aligning with results from the Allen Institute open access database, which
559 reports markedly low *PVALB* mRNA expression levels in some layer 2/3 pvalb cells (Fig 8B).

560 The patch-sequencing results closely aligned with the average mRNA profiles of pvalb neuron
561 types in the Allen Institute database (Fig 8B). The database confirmed the absence of *KCNA1*
562 expression in humans but not in mice ($p < 0.001$), as well as expression of *KCNA2* in both
563 species. It also confirmed that among the potassium channel genes analyzed, only Kv1 channel
564 genes were consistently expressed at lower levels in human pvalb neurons relative to mouse
565 neurons (one-way MANOVA with a *post hoc* Bonferroni test).

566 Kv1 channel blocker dendrotoxin lowers the AP firing threshold 567 more prominently in mouse neurons than in human neurons

568 We investigated whether Kv1 channel blockade through dendrotoxin-K (DTXK)
569 affects AP generation differently in human and mouse pvalb neurons [53, 58]. After 5 min of
570 baseline whole-cell current–clamp recording (conditions similar to those shown in Fig 1), slices
571 were exposed to 100 nM DTXK for 10 min, and AP threshold was remeasured (Fig 9A1, 2).
572 DTXK significantly lowered the AP firing threshold in human neurons from −38.8 mV (IQR
573 = −42.3 to −32.2 mV) to −40.0 mV (IQR = −45.3 to −37.2 mV; n = 10 cells; p = 0.004;
574 Wilcoxon signed-rank test with Bonferroni correction). In mouse cells, the reduction was from
575 −31.9 mV (IQR = −35.9 to −29.5 mV) to −40.7 mV (IQR = −45.8 to −38.2 mV; n = 10 cells;
576 p = 0.004; Wilcoxon signed-rank test with Bonferroni correction), and more prominent
577 compared to human cells (p = 0.019; Mann–Whitney U test with Bonferroni correction).

578 **Fig 9. Kv1 channel blocker dendrotoxin lowers AP threshold more prominently in mouse versus**
579 **human pvalb neurons.**

580 APs were recorded under baseline conditions (black traces) in current–clamp mode at −70 mV (as
581 shown in Fig 1) for 5 min, followed by application of 100 nM DTXK for 10 min, after which APs were
582 evoked again (red traces). (A) APs and corresponding AP phase plots in baseline control and after
583 DTXK application. (A1) Left: Three superimposed APs from a human pvalb cell. Right: Corresponding
584 phase plots under control and DTXK conditions. (A2) Left: Superimposed APs recorded in a mouse
585 pvalb neuron. Right: Corresponding AP phase plots. (B–E) Plots show average changes in AP
586 parameters measured at the AP threshold in human and mouse neurons (n = 10 cells each). Values
587 represent the difference between DTXK and baseline conditions. (B) DTXK induced a larger negative
588 shift in the AP firing threshold in mouse cells compared with human cells. (C) Reduction in rheobase
589 current following DTXK application was greater in mouse than in human cells. (D) DTXK caused a
590 more pronounced reduction in AP AHP in mouse compared with human cells. (E) No significant change
591 was observed in the AP maximum fall speed between species.

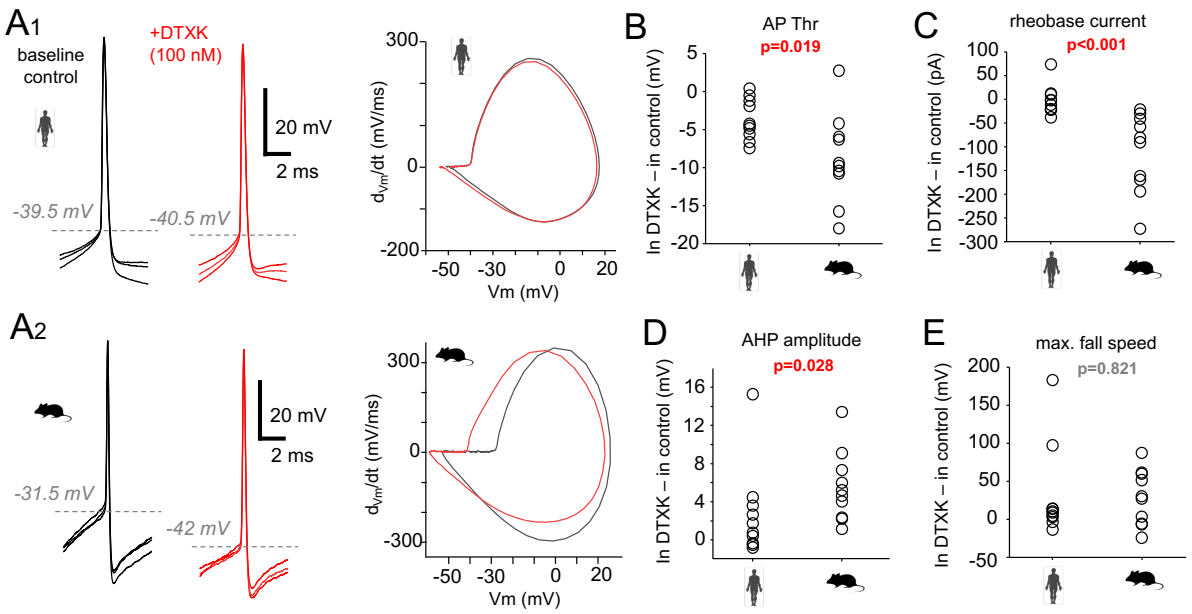

592

593 In both species the AP maximum fall speed was reduced (humans: p = 0.049; mice p = 0.020),
594 whereas in mice but not humans, the rheobase current decreased (human: p = 0.375; mice: p =

595 0.002) and the AHP amplitude declined (humans: p = 0.064; mice: p = 0.002; Wilcoxon signed-
596 rank test with Bonferroni correction). Other AP properties, Rin, and tau were unaffected. Full
597 results are provided in Table 2.

598 **Table 2. AP parameters, Rin, and tau in pvalb neurons under baseline and DTXK exposure**
599 **conditions.**

	Human n = 10			**Mouse n = 10**		
	Baseline median, (IQR)	**DTX, median, (IQR)**	**P-value (baseline vs. DTX)**	**Baseline median, (IQR)**	**DTX, median, (IQR)**	**P-value (baseline vs. DTX)**
AP Thr (mV)	−38.8 (−42.3 to −32.2)	−40.0 (−45.3 to −37.2)	**0.004**	−31.9 (−35.9 to −29.5)	−40.7 (−45.8 to −38.2)	**0.004**
Initial rise slope (ms^{-1})	39.1 (33.0 to 44.5)	41.0 (30.2 to 57.9)	0.492	45.9 (38.3 to 57.5)	49.6 (42.1 to 79.8)	0.275
AP ampl (peak value − SpkThr, mV)	56.4 (46.3 to 61.4)	52.6 (42.9 to 59.8)	0.432	57.6 (44.4 to 62.7)	62.8 (33.5 to 70.0)	0.922
AP half width (ms)	0.54 (0.43 to 0.77)	0.55 (0.46 to 0.87)	0.426	0.35 (0.30 to 0.60)	0.36 (0.32 to 0.63)	0.770
AP rheobase (pA)	83.4 (37.1 to 113.1)	77.6 (45.9 to 104.8)	0.375	280.3 (135.5 to 443.6)	121.9 (94.0 to 283.7)	**0.002**
AP latency (ms)	23.3 (20.5 to 32.1)	26.6 (17.0 to 52.7)	0.922	71.8 (37.1 to 124.0)	27.8 (12.4 to 86.6)	0.160
Spike number by step	2.6 (1.0 to 6.9)	2.1 (1.8 to 5.1)	0.742	4.2 (2.7 to 10.0)	5.0 (2.3 to 9.5)	0.770
AP AHP ampl (mV)	−16.6 (−12.7 to −18.6)	−13.6 (−10.4 to −17.2)	0.064	−18.4 (−15.2 to −21.1)	−13.4 (−8.2 to −14.8)	**0.002**
Max rise speed (mV/ms)	232.8 (151.7 to 328.9)	226.8 (118.8 to 342.7)	0.375	331.2 (233.7 to 373.2)	342.4 (132.8 to 419.1)	0.770
Max fall speed (mV/ms)	−140.6 (−168.5 to −97.9	−127.6 (−154.5 to −53.6)	**0.049**	−162.4 (−229.7 to −108.0)	−98.2 (−234.1 to −61.0)	**0.020**
Rin (MΩ)	226.5 (94.8 to 455.1)	244.7 (116.1 to 402.3)	0.432	90.3 (82.4 to 199.8)	96.5 (76.6 to 173.0)	0.492
Tau (ms)	6.8 (4.5 to 8.4)	7.0 (5.1 to 8.0)	0.770	4.7 (3.6 to 6.9)	4.7 (4.1 to 5.9)	0.695

600 Rin: cell input resistance; tau: membrane time constant, measured as the voltage response to a +10-
601 mV step from −70 mV. Data are presented as medians with quartiles. P-values indicate differences
602 within each species before and after DTXK exposure (Wilcoxon signed-rank test with Bonferroni
603 correction).

604

605 Species comparisons of DTXK-induced changes in significantly affected AP parameters (Fig
606 9B–E) revealed that threshold shift ($p = 0.019$), rheobase reduction ($p < 0.001$), and AHP
607 amplitude decrease ($p = 0.028$) were all greater in mouse cells compared with human cells,
608 whereas the reduction in AP maximum fall speed was comparable between species ($p = 0.821$;
609 Mann–Whitney U test with Bonferroni correction).

610 Fast-spiking neuron computational model with a human-type AIS 611 reveals a lowered firing threshold and shortened time lag to AP 612 generation

613 We established a single-cell computational model with axonal and dendritic cable
614 properties and an AIS replicating the electrical characteristics of human pvalb neurons. We
615 simulated the effects of species-specific AIS differences, namely AIS length and Kv1 channel
616 content, on AP firing threshold and the time lag between somatic excitation and AP initiation.
617 The model's intrinsic properties were tuned to match the Vm waveforms and AP firing
618 threshold observed in human pvalb cells during voltage step protocols (Fig 10A1, 2).
619 Specifically, the model reproduced a whole-cell recorded human pvalb cell (code h7, Table S1)
620 with Hodgin–Huxley-type APs and incorporated voltage-sensitive low-threshold Na^+ current
621 (Nav1.6 in the AIS), high-threshold Na^+ current (Nav1.2 in the soma and proximal dendrites),
622 and K^+ currents (Kv3.1 and Kv3.2 in the AIS, soma, and dendrites). The soma and dendrites

623 also included voltage-insensitive K^+ leak current, M-type and Kir-type K^+ currents [63], and
624 hyperpolarization-activated nonspecific cation Ih current [28]. Variable Kv1 activity
625 (conductance) was applied in the AIS. Under standard conditions, the AIS length was 20 μm,
626 initiation distance from the soma was 10 μm, and the AP firing threshold was −43 mV.

627 **Fig 10. Fast-spiking neuron computational model with human or mouse AIS.**

628 (A) Single-cell computational model with axon and dendrite cable properties replicating the human
629 pvalb cell's somatic electrical behavior. (A1) Vm responses in a real human pvalb neuron (blue) and
630 the model cell (gray) to current steps from −200 to +200 pA. (A2) Left: First AP elicited by the lowest
631 suprathreshold step in the real neuron (blue) and model cell (gray). Right: Corresponding AP phase
632 plots. (B) Increasing AIS length from 10 to 30 μm, within the observed range in real pvalb cells, lowered
633 the AP firing threshold in the model (Kv1 and Nav1.6 channel conductance = 20 nS/μm^2, AIS-to-soma
634 distance = 10 μm, axon Ra = 0.9 MΩ·μm, axon diameter = 0.8 μm). (B1) Model APs and phase plots
635 with AIS lengths of 10 μm (purple) and 30 μm (red). (B2) AP firing threshold simulated for AIS lengths
636 of 10 μm (purple), 20 μm (brown), and 30 μm (red) (illustrated in schematic inset). Threshold sensitivity
637 was highest at 10–20 μm, a range common to both human and mouse pvalb neurons in reality. (C)
638 Reducing Kv1 channel activity in the AIS lowered the AP firing threshold in the model. (C1) Model
639 APs and phase plots at different Kv1 conductances in the AIS: gKv1 = 0 (yellow) and 15 nS/μm^2 (red).
640 (C2) AP firing threshold at Kv1 conductance levels of 0, 5, 10, and 15 nS/μm^2 (abscissa; Nav1.6
641 conductance = 20 nS/μm^2, AIS length = 20 μm, AIS-to-soma distance = 10 μm). (D) Combined AIS
642 elongation and reduced Kv1 activity synergistically lowered the AP threshold in the model. Heatmap
643 illustrates the combined effect of AIS length (abscissa) and Kv1 conductance (ordinate) on the AP firing
644 threshold (color scale, right). Total AP threshold range across conditions was 11 mV. (E–G) Human-
645 type AIS shortened the AP generation lag. (E) Real human and mouse neurons differed in depolarization
646 kinetics and AP thresholds but showed similar AP generation lags. Human pvalb neuron (blue) had a
647 slower membrane depolarization (E1) and lower AP threshold (E2) relative to the mouse pvalb neuron
648 (gray). (E3) AP generation lag, defined from the onset of a depolarizing step (black dotted lines) to AP

649 initiation (gray dotted lines) in four representative traces (AP onset defined at 10-mV/ms rise speed).
650 (E4) AP generation lag versus excitatory current steps in the soma of human (blue) and mouse (gray)
651 neurons. Human neuron fired with a lower current (abscissa; vertical dotted lines) but showed a similar
652 time lag (horizontal dotted line) relative to the mouse neuron. (F) Switching AIS properties in the model
653 from mouse-like to human-like reduced the AP generation lag to somatic excitation. (F1) The human-
654 type AIS lowered the AP threshold in response to simulated EPSCs in the model neuron soma. Vm
655 traces showed excitatory postsynaptic potentials (EPSP) of increasing strength that eventually triggered
656 an AP in model neurons with human (blue) and mouse (gray) AIS. EPSP-generating conductances with
657 peak amplitudes of 6–nS are presented on the left (black traces). Scale bars: 40 ms and 50 mV. (F2)
658 Human-type AIS shortened the AP generation lag in response to EPSPs. Vm traces showed APs
659 triggered by equal-strength excitatory postsynaptic currents (EPSC) (8.5-nS peak conductance) in
660 model neurons with human-type (blue) or mouse-type (gray) AIS. (F3) AP generation lag in the model
661 cell plotted against increasing EPSC conductance in model neurons with human-type (blue dots) and
662 mouse-type (gray dots) AIS. Response to the 8.5-nS EPSC is highlighted in red. (G) Heatmap showing
663 the combined effect of AIS length (abscissa) and AIS Kv1 conductance (ordinate) on the AP generation
664 time lag in response to a fixed-strength EPSC (8.5 nS) in the model neuron. Color scale (right) indicates
665 time lag in milliseconds.
666

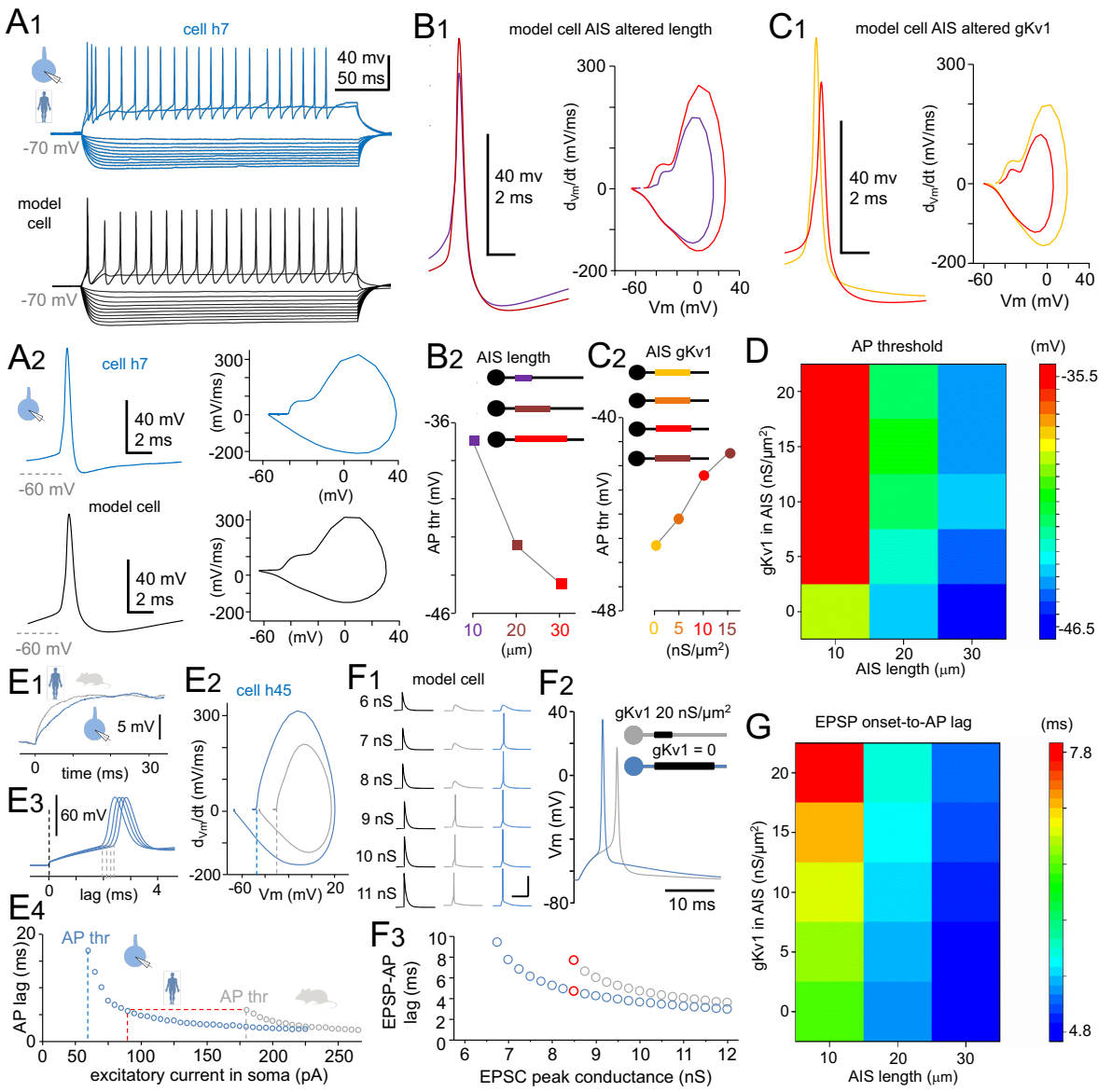

First, we simulated the AP firing thresholds by varying AIS lengths (10–30 μm), within the anatomical range observed in real pvalb neurons. Increased AIS length linearly scaled Nav1.6 and Kv1 channel activity in the AIS (conductances: gNav1.6 and gKv.1 = 20 nS/μm^2). The axon diameter was 0.8 μm, with a longitudinal resistance (Ra) of 0.9 MΩ·μm. Increasing AIS length from 10 to 20 and 30 μm lowered the AP firing threshold (elicited by a 250-ms square-pulse current at the soma of −70 mV) from −36.8 to −42.3 and −45.2 mV, respectively (Fig 10B1, 2), demonstrating that AIS length (with fixed gNav1.6 and gKv.1 per μm^2) strongly modulates AP threshold.

676 Next, we examined how varying Kv1 conductance in the AIS affects AP threshold while fixing
677 the AIS length (20 μm), location along the axon (10 μm from the soma, Ra = 0.9 MΩ·μm),
678 and gNav1.6 density (20 nS/μm^2). Depolarizing steps were applied to elicit APs. Increasing
679 gKv1 from 0 to 5, 10, and 15 nS/μm^2 in the AIS (Fig 10C1, 2) raised the AP threshold from
680 −45.3 to −44.2, −42.4, and −41.6 mV, respectively (Fig 10D). This simulation confirmed that
681 Kv1 conductance in the AIS increases firing threshold independently of AIS geometry. We
682 also simulated increased Nav1.6 conductance in the AIS, and found that it effectively reduced
683 AP threshold in the model cell (Fig S1A).

684 We then ran simulations incorporating cell-to-cell variability parameters shared across species.
685 With fixed AIS length (20 μm) and channel conductances (gNav1.6 and gKv1 = 20 nS/μm^2),
686 we varied the AIS initiation site distance (0 or 10 μm from the soma). AP threshold was lower
687 when AIS was 10 μm from the soma (−43.2 mV) compared with 0 μm (−41.5 mV; Fig S1B,
688 C). We also simulated the impact of axon diameter variation (0.6–0.9 μm), which alters both
689 the Ra (0.8–1.1 MΩ·μm) and extracellular membrane surface area (calculated as diameter × π,
690 with gNav1.6 and gKv1 = 20 nS/μm^2). Narrower axons (0.6 μm) with higher Ra (1.1 MΩ·μm)
691 yielded the lowest AP threshold (−44.7 mV) in the model cell, whereas wider axons (0.9 μm)
692 with lower Ra (0.8 MΩ·μm) had the highest threshold (−42.2 mV). Varying Ra alone (with a
693 fixed axon surface area) shifted the threshold by <1 mV; changing surface area alone (while
694 keeping Ra constant), thereby increasing total ion channel conductance, altered the threshold
695 by ~2 mV. Notably, when axon diameter was increased over the range observed in the
696 anatomical study, thereby lowering Ra while increasing total Nav1.6 and Kv1 channel
697 conductance, the AP firing threshold moderately increased only by ~2.5 mV. These
698 relationships are detailed in the heatmap shown in Fig S1A–C.

699 Finally, we used the model cell to explore how AIS-dependent changes in firing threshold
700 influence the time lag between EPSC onset AP generation in pvalb neurons. The simulation
701 aimed to address why human pvalb neurons, compared with mouse pvalb neurons, despite
702 having a slower somatic membrane tau (Fig 10E1) and a lower AP firing threshold (Fig 10E2),
703 can generate APs with an equal or shorter time lag in response to a fixed-amplitude excitatory
704 current in the soma (Fig 10E3, 4) [38]. In the model neuron, we generated an EPSC in the soma
705 at −70 mV and incrementally increased its peak amplitude to evoke a gradually increasing
706 EPSP that eventually reached the AP firing threshold [28]. The EPSC was applied with peak
707 conductance values from 6 to 11 nS in steps of 0.25 nS, reaching the AP firing threshold with
708 the human- and mouse-type AIS configurations at EPSC conductances of 6.75 and 8.50 nS,
709 respectively (Fig 10F1–3). Shifting from the "mouse-type AIS" (Kv1 density = 20 nS/μm^2,
710 AIS length = 10 μm) to the "human-type AIS" (Kv1 density = 0 nS/μm^2, AIS length = 30 μm)
711 resulted in a shorter time lag to AP generation when the EPSC strength was fixed (Fig 10F2,
712 3). The EPSP–AP time lag simulation with varying AIS lengths and Kv1 densities is shown in
713 a heatmap in Fig 10G. The simulation revealed a range of AP generation time lags from 4.8
714 and 7.8 ms in response to a fixed EPSC strength (8.5 nS, corresponding to the AP threshold in
715 the mouse-type AIS). Overall, these simulations demonstrate that the lower AP firing threshold
716 associated with the human-type AIS compared to the mouse-type AIS in pvalb cells is
717 accompanied by a shorter time lag to AP generation in response to synaptic current at the soma.

718 Discussion

719 Species-specific traits in organs, tissues, and cells have evolved in response to selection
720 pressure during phylogenetic evolution [8, 64, 65]. Consequently, homologous cell types (i.e.,
721 neurons expressing the same cell-type specific marker genes) are broadly conserved across
722 mammalian species but still exhibit interspecies differences that reflect adaptations for

723 functional advantages [4, 66-69]. Our findings suggest that fast-spiking pvalb neurons in the
724 human neocortex evolved a lower AP firing threshold to support their role as fast in–fast out
725 circuits. This enhanced input-to-output signal transformation speed is especially important in
726 human neurons, which have electrically slower somata compared with rodent neurons.
727 Molecular, anatomical, and pharmacological data, together with model simulations, showed
728 that the reduced AP threshold in human pvalb neurons results from diminished Kv1 inhibitory
729 potassium channel content in the AIS and an elongated AIS.

730 Low AP firing threshold helps electrically slower human 731 interneurons to function as fast in–fast out circuits

732 A short delay in AP generation in response to excitatory synaptic input (i.e., input–
733 output transformation) is a key feature of fast-spiking pvalb interneurons in the cortex across
734 mammals [40, 43]. These neurons, the most numerous inhibitory population in the cortex [6,
735 70, 71], exert fast, temporally precise inhibition on various other neuron types [43]. In the
736 human neocortex, rapid signal transformation poses a challenge for many pvalb neurons owing
737 to their slower somatic membrane potential kinetics. However, a lowered AP threshold
738 compensates for this, reducing the time lag in input–output transformation. This helps preserve
739 the archetypical fast in–fast out function of pvalb neurons in humans, as demonstrated through
740 our computational model.

741 Slowed inhibitory signaling in the human neocortex would be detrimental, as theoretical
742 models and *in vivo* animal studies have linked such changes to reduced cortical computation
743 speed and cognitive impairment [40, 72-75]. Therefore, human fast-spiking interneurons have
744 evolved distinct adaptations that maintain rapid electrical input–output transformations. These
745 include simplified dendritic morphology that facilitates synaptic potential propagation from
746 distal dendrites to the soma [2, 31]. Moreover, human pvalb neurons express more voltage-

747 sensitive excitatory cation channels in the soma and proximal dendrites to accelerate membrane
748 potential dynamics [28]. We also observed an adaptation in AP generation at the soma. Some
749 of these features likely generalize to primate pvalb neurons, as macaque neocortical neurons
750 also exhibit slower Vm kinetics and reduced AP thresholds compared with rat neurons [36].

751 Why do human pvalb neurons have electrically slower somata 752 relative to rodent neurons?

753 The slower soma membrane dynamics in human pvalb neurons result from increased
754 cell Rin, which reflects reduced transmembrane ion leakage. This is supported by findings
755 showing that cell Cm, a parameter that combines with Rin to determine membrane tau, is
756 similar between primate and rodent fast-spiking neurons [36, 37]. In mice, somatic tau
757 correlates with Rin, but in humans, this link is weak, indicating high variability in membrane
758 ion channel density between individual human neurons (hence, in electrical resistivity per
759 plasma membrane area), which governs ion leakage [76].

760 The reason high Rin evolved in human pvalb neurons remains unclear, as it is inherently
761 unfavorable for fast in–fast out function. One hypothesis is that evolutionary pressure favored
762 neurons that produce Vm changes with reduced electric current demands, minimizing
763 transmembrane ion flux to conserve metabolic energy [77, 78]. Fast-spiking interneurons are
764 energetically demanding [79-81], and their metabolic cost may be heightened in the human
765 brain due to the higher proportion of interneurons in the cortex compared with that in rodents
766 [14, 82, 83]. However, the increased electrical resistivity of the plasma membrane in human
767 pvalb neurons likely necessitated an adjustment of the AP threshold to preserve their rapid
768 electrical input–output transformation.

769 **Mechanisms underlying the lowered firing threshold in human**
770 **fast-spiking neurons**

771 Experiments using a Kv1 channel blocker directly demonstrated the strong role of Kv1
772 channels in setting a higher AP threshold in mouse pvalb neurons compared with human pvalb
773 neurons. Immunofluorescence analysis revealed a deficiency of Kv1.1 channels in human
774 neocortical pvalb neurons, and *KCNA1* expression was absent in all human pvalb neurons,
775 despite being present in mouse cells. These findings aligned with results from the Allen
776 Institute transcriptomic database on averaged mRNA levels in human and mouse pvalb neuron
777 subtypes. Although Kv1.2 channels were similarly expressed in both species, immunostaining
778 showed weak AIS labeling in each, and the Allen Institute dataset indicated lower average
779 Kv1.2 levels in human-type compared with mouse-type pvalb cells. However, the combined
780 mRNA levels of Kv1.1 and Kv1.2 did not correlate with AP threshold across individual cells.
781 Larger datasets in future studies may help clarify this relationship. Both datasets showed that
782 the Kv1 channel gene group was the only potassium channel group expressed at lower levels
783 in human pvalb neurons compared with mouse neurons. We argue that species differences in
784 Kv1.1 channel density are the major determinant of the lower AP threshold in humans.
785 Although this work does not determine the exact AP initiation site in the AIS, it shows that the
786 low-threshold ion channels Nav1.6 and Kv1 are, on average, evenly distributed along the AIS,
787 without a consistent intensity peak at either end.

788 Human pvalb neurons have a longer AIS on average relative to their mouse counterparts, and
789 simulations showed that AIS length strongly modulates AP threshold within the physiological
790 range observed. AIS length appears to contribute to AP threshold variability across individual
791 pvalb cells in both species and helps partly explain the interspecies difference. The large cell-
792 to-cell variability of AIS length and localization was also evident in the correlation between

AP threshold and AIS structure within the same cells: due to the variability in both measures, the results remained less clear and partially diverged from the correlation findings in the larger, independent datasets.

AIS elongation lowers the AP threshold by increasing the total number of Na channels in the initial segment [41, 48], and this effect is especially pronounced in human AIS with low inhibitory Kv1 channel content. Increasing AIS length reduces AP threshold more effectively than expanding axon diameter, although both increase the number of AIS ion channels. However, expanding axon diameter also lowers Ra, which shifts AP threshold in the opposite direction and limits its effect [48]. In rodents, AIS elongation coincides with changes in voltage-gated potassium channel composition to enhance excitability [45]. Human pvalb neurons similarly exploit both geometry and reduced Kv1 activity to lower AP threshold.

Mechanisms underlying cell-to-cell variability in the AP threshold without interspecies differences

The distance from the AIS initiation site to the soma, the axon diameter, and the axon Nav1.6 channel immunofluorescence intensity vary across individual neurons but do not account for the species difference in AP threshold. However, these features likely contribute to cell-to-cell variability in pvalb neuron AP thresholds in both species, as indicated by our model cell simulations.

Increases in axon diameter [48] typically occur with reduced Ra, which raises the AP threshold in pvalb interneurons. Given the evolutionary pressure to lower the AP threshold in human neurons, it follows that axon diameter in human pvalb neurons is not markedly larger than that in mouse cells, as enlargement would counteract AP threshold reduction.

The AIS is not a static cellular microdomain [84], and the observed cell-to-cell variability in AIS properties likely results from plasticity mechanisms [85], enabling the brain to adapt, learn,

817 and repair. Whether these mechanisms differ between humans and animal models remains
818 unknown.

819 Conclusions

820 Results and conclusions regarding neocortical neural networks are likely influenced by
821 species-specific neuronal features. Studies that rely solely on animal models may provide an
822 inaccurate picture of human brain network physiology and aging. The same concerns apply to
823 degenerative mechanisms underlying disease processes. Therefore, identifying human-specific
824 neural features is crucial to developing effective therapeutic strategies for degenerative brain
825 conditions, in which PVALB neurons are often emphasized.

826 Study limitations

827 The lack of biotechnological tools to selectively and rapidly manipulate gene
828 expression, and consequently the AIS ion channel composition and microstructure, in
829 genetically defined neuron types, such as pvalb neurons, in human brain slices continues to
830 constrain experimental design. In addition, immunostaining-based localization and
831 quantification of proteins are limited by antibody validation, which currently relies on
832 knockouts only feasible in nonhuman species. Future availability of such techniques in human
833 tissue will enable a more detailed understanding of the human-type AIS in health and disease.

834 Materials and Methods

835 Ethics statement and licenses

836 All procedures were approved by the University of Szeged Ethics Committee, the
837 Regional Human Investigation Review Board (ref. 75/2014), and the Scientific and Research
838 Ethics Committee (ETT TUKEB) BM/25042-1/2024 and were conducted in accordance with
839 the tenets of the Declaration of Helsinki. Written informed consent was obtained from all

840 patients before surgery. For underage patients, consent was obtained from a parent or
841 guardian.

842 Human brain slices

843 Neocortical slices were prepared from frontal, temporal, or other cortical samples
844 resected during deep-brain surgeries. Patients ranged in age from 11 to 85 years, and samples
845 were obtained from both hemispheres of male and female patients (Table S1). Anesthesia was
846 induced with intravenous midazolam (0.03 mg/kg) and fentanyl (1–2 μg/kg) after a bolus
847 intravenous injection of propofol (1–2 mg/kg). Rocuronium (0.5 mg/kg) was administered to
848 facilitate endotracheal intubation. During surgery, patients were ventilated with a 1:2 O_2/N_2O
849 mixture, and anesthesia was maintained with sevoflurane. After resection, tissue blocks were
850 immediately immersed in an ice-cold solution containing (in mM) 130 NaCl, 3.5 KCl, 1
851 NaH_2PO_4, 24 $NaHCO_3$, 1 $CaCl_2$, 3 $MgSO_4$, and 10 d-(+)-glucose, which was aerated with 95%
852 O_2/5% CO_2 in a glass container. The container was kept on ice in an insulated box and
853 transported within 20 min to the electrophysiology laboratory under continuous aeration (95%
854 O_2/5% CO_2). Slices (350-μm thick) were cut using a vibrating blade microtome (Microm HM
855 650 V, Thermo Fisher Scientific, Cambridge, UK) and incubated for 1 h at 22°C–24°C in
856 slicing solution. This solution was gradually replaced by recording solution (180 mL) delivered
857 at 6 mL/min by pump. The recording solution matched the slicing solution except for 3 mM
858 $CaCl_2$ and 1 mM $MgSO_4$.

859 Mouse brain slices

860 Transverse slices (350 μm) were prepared from the somatosensory (n = 45) and frontal
861 (n = 50) cortices of 5–7-week-old heterozygous B6.129P2-Pvalbtm1(cre)Arbr/J mice (stock
862 017320, B6 PVcre line; Jackson Laboratory, Bar Harbor, ME, USA) crossed with Ai9 reporter
863 mice to express the tdTomato fluorophore in pvalb GABAergic neurons, which aided cell

selection. Cells were tentatively identified electrophysiologically through fast spike kinetics and high-frequency, nonaccommodating firing in response to 500-ms suprathreshold depolarizing pulses [38].

Electrophysiological recordings and data analysis

Recordings were performed in a submerged chamber perfused at 8 mL/min with recording solution maintained at 36°C–37°C. Cells were patched under visual guidance using infrared differential interference contrast video microscopy with a water-immersion ×20 objective, additional zoom (up to ×4), and a dichroic mirror and filter (Cy3) for TdTomato fluorescence in mouse tissue. All recordings were conducted within 30 min of entering whole-cell mode. Micropipettes (5–8 MΩ) were filled with intracellular solution containing (in mM) 126 K-gluconate, 8 NaCl, 4 ATP-Mg, 0.3 Na_2-GTP, 10 HEPES, and 10 phosphocreatine (pH 7.0–7.2; 300 mOsm) supplemented with 0.3% (w/v) biocytin for *post hoc* staining with fluorophore-conjugated streptavidin. Recordings were performed with a Multiclamp 700B amplifier (Axon Instruments, Scottsdale, AZ, USA) and low-pass–filtered at 6–8 kHz (Bessel filter). Series resistance and pipette capacitance were compensated in current–clamp mode. Vm values were not corrected for the liquid junction potential. Somatic tau was measured in current–clamp mode with +10 mV Vm steps (250–500 ms) from −70 mV. AP threshold was measured in dV/dt versus Vm phase plots as the Vm at which AP rise speed reached 10 mV/ms [31, 44]. All parameters were based on at least five traces. Data were acquired with Clampex software (Axon Instruments), digitized at 35–50 kHz, and analyzed offline using pClamp (v10.5; Axon Instruments), Spike2 (v8.1; Cambridge Electronic Design, Milton, UK), OriginPro (v9.5; OriginLab Corporation, Northampton, MA, USA), and SigmaPlot (v14; Grafiti, Palo Alto, CA, USA).

Drugs

888 Brain slices were perfused with 100 nM dendrotoxin-K (Cat. No. D4813,
889 Merck/Sigma-Aldrich).

890 Tissue fixation and cell visualization

891 Cells loaded with biocytin during whole-cell patch-clamp recordings were visualized
892 using Alexa 488–conjugated streptavidin (1:1000) or Cy3-conjugated streptavidin (1:1000;
893 both Jackson ImmunoResearch, West Grove, PA, USA). Immediately following recordings,
894 slices were fixed in 4% paraformaldehyde and 15% picric acid in 0.1 M phosphate buffer (PB;
895 pH 7.4) at 4°C for at least 12 h, followed by storage at 4°C in 0.1 M PB containing 0.05%
896 sodium azide as a preservative. All slices were embedded in 20% gelatin and cut into 50-µm-
897 thick sections using a vibratome (VT1000S, Leica Microsystems, Wetzlar, Germany) in ice-
898 cold PB. Sections were rinsed in 0.1 M PB (3 × 10 min), cryoprotected in 10%–20% sucrose
899 in 0.1 M PB, flash-frozen in liquid nitrogen, and thawed in 0.1 M PB. Slices were then
900 incubated in 0.1 M Tris-buffered saline (TBS; pH 7.4) containing fluorophore-conjugated
901 streptavidin for 2 h 30 min at 22°C–24°C, rinsed in 0.1 M PB (3 × 10 min), mounted in
902 Vectashield mounting medium (Vector Laboratories, Burlingame, CA, USA), placed under
903 coverslips, and examined under an epifluorescence microscope (Leica DM 5000 B, Milton
904 Keynes, UK) at ×20–60 objectives.

905 For single-cell reconstructions, selected sections were incubated overnight at 4°C in a
906 conjugated avidin–biotin horseradish peroxidase solution (1:300; Vector Labs) in TBS (pH
907 7.4). The enzyme reaction was developed using the glucose oxidase–DAB–nickel method with
908 3′3-diaminobenzidine tetrahydrochloride (0.05%) and 0.01% H_2O_2 as the chromogen and
909 oxidant, respectively. Sections were postfixed in 1% OsO_4 in 0.1 M PB, rinsed in distilled
910 water, and stained with 1% uranyl acetate. Dehydration was performed in a graded ethanol
911 series, followed by overnight infiltration with epoxy resin (Durcupan, Merck kft., Budapest,

912 Hungary) and mounting on glass slides. Light microscopic reconstructions were performed
913 with the Neurolucida system (MBF Bioscience, Williston, VT, USA) using a ×100 objective
914 (Olympus BX51, Olympus UPlanFI, Olympus, Tokyo, Japan). Images were collapsed along
915 the z-axis for presentation.

916 Immunohistochemistry

917 Free-floating sections were washed in TBS containing 0.3% Triton-X (TBST) three
918 times over 1 h at 20°C–24°C, followed by incubation in a blocking solution containing 20%
919 horse serum in TBST. Antigen retrieval was performed by treating the slices with 1 mg/mL
920 pepsin (catalog #S3002; Dako, Glostrup, Denmark) in 1 M HCl with 0.1 M PB at 37°C for 5–
921 6 min, followed by rinsing in 0.1 M PB. Sections were then incubated with primary antibodies
922 diluted in TBST for three nights at 4°C with corresponding fluorochrome-conjugated
923 secondary antibodies (2% blocking serum in TBST) overnight at 4°C. Between antibody
924 incubations, sections were washed in TBST (3 × 15 min), followed by rinses in 0.1 M PB (2 ×
925 10 min). Slices were then mounted on glass slides with Vectashield mounting medium (Vector
926 Laboratories) for imaging.

927 The following primary antibodies were used for immunolabeling: goat anti-pvalb (1:1000;
928 PVG-213, Swant, Burgdorf, Switzerland), mouse anti-spectrin beta-4 (1:100; Invitrogen,
929 Thermo Fisher Scientific, Waltham, MA, USA), rabbit anti-Nav1.6 (SCN8A, 1:300; Alomone
930 Labs, Jerusalem, Israel), rabbit anti-Kv1.1 (KCNA1, 1:100; Alomone Labs), and rabbit anti-
931 Kv1.2 (KCNA2 APC-010, 1:100; Alomone Labs). Prior to confocal microscopy observations,
932 immunolabeling was visualized using the following secondary antibodies: DAM Alexa 488–
933 conjugated donkey anti-mouse (1:400; Jackson ImmunoResearch), DARb Cy3-conjugated
934 donkey anti-rabbit (1:400; Jackson ImmunoResearch), and DaGt A647-conjugated donkey
935 anti-goat (1:200; Thermo Fisher Scientific). Immunoreactivity was evaluated using an

936 epifluorescence microscope with a quasiconfocal option (Zeiss ApoTome 2, Zeiss,
937 Oberkochen, Germany).

938 Immunofluorescence image acquisition and analysis

939 Immunofluorescently labeled sections were imaged using a Leica Stellaris 8 laser-
940 scanning confocal microscope (Leica Microsystems, Biomarker Kft. Budapest, Hungary) with
941 499-, 554-, and 649-nm lasers to excite the fluorophores, using 504–553-, 559–654-, and 654–
942 750-nm emission filters, respectively.

943 To quantify immunofluorescence around the soma, 24 radial measurement lines (50 pixels/µm)
944 were placed on the soma such that all lines projected radially from its center into the
945 extracellular space. Immunofluorescence intensity for pvalb (Cy5) and one of the three ion
946 channels (Cy3) was measured along radial lines in single-plane confocal images of the cell
947 soma. The location of the extracellular membrane was defined by the onset of the pvalb signal
948 when moving from the extracellular to the intracellular position along each line. This position
949 was marked as 0 and defined as follows: (average extracellular fluorescence pixel value −
950 average intracellular fluorescence pixel value) / 2. For pooled analysis, all lines were aligned
951 at this 0-point.

952 Ion channel fluorescence from the extracellular space (recorded from the 24 radial lines−3.0 to
953 −0.5 µm relative to the 0-point, in total ca. 3000 pixels per cell) was averaged and used as a
954 specific reference signal for each cell. This average extracellular value was subtracted from
955 pixel intensities at the membrane (−0.5 to +0.5 µm from the 0-point) and in the intracellular
956 cytoplasm (+0.5 to +1.5 µm from the 0-point). The extracellular site fluorescence (average
957 intensity) did not differ significantly between species (Kv1.1, n = 31 cells, p = 0.06; Kv1.2, n
958 = 32 and 59, p = 0.835, Mann–Whitney U test). The intracellular measurement zone was chosen
959 near the extracellular membrane to sample the cytoplasm while avoiding the nucleus, which

960 was not visualized in staining. For axonal analysis, the same extracellular reference value (from
961 24 lines per cell) was subtracted from fluorescence intensity measurements pixels along the
962 axonal lines.

963 Z-stack images were acquired from the same cells using a HC PL APO CS2 63×/1.40 oil
964 immersion objective in unidirectional scanning mode. Axonal fluorescence measurement lines
965 were sampled at 50 pixels/µm. AIS immunofluorescence in z-stack images was analyzed using
966 a custom ImageJ macro (US National Institutes of Health, Bethesda, MD, USA) and a script
967 developed by Dr. Adam Tiszlavicz [86] to determine the AIS's length and its proximal and
968 terminal points (visualized via beta-IV-spectrin immunoreaction). This was achieved by
969 manually marking the points and applying the Euclidean distance formula. Fluorescence
970 intensity was then measured along a polyline connecting these points, capturing the full signal
971 profile of the immunolabeled channels. AIS lengths were normalized by dividing into 10 bins
972 (from proximal to distal). Ion channel immunoreactivity (Cy3) was measured in parallel with
973 pvalb (Cy5) and beta-IV-spectrin (Alexa 488), and axonal fluorescence values were referenced
974 to the average extracellular signal of the corresponding cell, using the same normalization
975 approach applied for somatic radial lines.

976 Nucleus collection for patch-sequencing

977 Nuclei were collected from cells exhibiting a fast-spiking phenotype. Prior to data
978 collection, all surfaces, equipment, and materials were thoroughly cleaned using DNA
979 AWAY™ (Thermo Fisher Scientific) and RNaseZap™ (Sigma-Aldrich, St. Louis, MO, USA).
980 The perfusion system was flushed with 50 mL of 70% ethanol. Following electrophysiological
981 recording, the pipette was centered on the soma and a small, constant negative pressure was
982 applied to extract the cytosol and draw the nucleus toward the tip. The pipette was slowly
983 retracted under continuous negative pressure while monitoring seal integrity. Once the nucleus

984 appeared at the pipette tip, retraction was accelerated to fully withdraw the pipette from the
985 slice. The pipette containing the internal solution, cytosol, and nucleus was removed from the
986 holder and expelled into a 0.2-mL tight-lock PCR tube (TubeOne, StarLab, Hamburg,
987 Germany) preloaded with 2 µL of lysis buffer comprising 0.8% Triton X-100; (Sigma-Aldrich)
988 and 1 U/µL RNase inhibitor (Takara, Kyoto, Japan). The internal solution contained the
989 following: 110 mM K-gluconate (Sigma-Aldrich), 4 mM KCl solution, RNase-free
990 (Invitrogen), 10 mM HEPES solution (Sigma-Aldrich), 1 mM ATP-Mg (Sigma-Aldrich), 0.3
991 mM GTP-Na (Sigma-Aldrich), 10 mM sodium phosphocreatine (Sigma-Aldrich), 0.2 mM
992 EGTA (Sigma-Aldrich), 20 µg/mL RNA-grade glycogen solution (Thermo Fisher Scientific),
993 and 0.5 U/µL RNase inhibitor (Takara). The 4-µL sample was briefly spun (2 s), placed on dry
994 ice, and stored at −80°C until in-tube reverse transcription.

995 cDNA amplification and library construction

996 Libraries were prepared using a protocol based on Smart-seq2 [87, 88]. Briefly, cDNA
997 was generated and amplified using 24 PCR cycles for all samples, including negative controls.
998 Indexes and adapter sequences were added to the cDNA, which was pooled equimolarly and
999 sequenced on an Illumina MiSeq platform (San Diego, CA, USA) in 50-bp single-end read
1000 mode. Each sample was sequenced to a depth of ~1–2 million reads.

1001 Sequencing data processing

1002 Sequencing used 66-bp paired-end reads aligned to the GRCh38 reference genome with
1003 annotation file GRCh38_r93 from Ensembl. Alignment was performed using STAR v2.7.11a
1004 [89] with the following parameters: --soloType SmartSeq --soloUMIdedup Exact --soloStrand
1005 Unstranded --soloFeatures GeneFull. Full gene counts, including introns and exons, produced
1006 via STAR were used to compute TPM values for downstream analysis.

Identification of pvalb neurons based on single-nucleus transcriptomics

Single-nucleus transcriptomic data were analyzed using the Allen Institute's MapMyCells tool (Allen Institute for Brain Science, 2024; RRID:SCR_024672, https://knowledge.brain-map.org/mapmycells/process/). This tool uses gene expression signatures to assign neurons to cortical cell types, enabling identification of pvalb neurons even when *PVALB/pvalb* expression is undetectable (Fig S1). For human cells, classification used the Seattle Alzheimer's Disease Brain Cell Atlas reference taxonomy with the Deep Generative Mapping algorithm; for mouse cells, the 10X Whole Mouse Brain reference taxonomy was employed with the hierarchical mapping algorithm. Only cells classified as pvalb neurons at $p > 0.9$ (supertype_bootstrapping_probability) were retained for further analysis. Human single-nucleus gene expression profiles showed strong concordance with the Allen Institute's high-resolution reference dataset for pvalb subtypes (subclass correlation coefficient > 0.5 using the 10X Whole Human Brain dataset and correlation mapping algorithm; Fig 8).

Single-cell model

The three-compartment neuron model included cylindrical dendritic and axonal compartments and followed a previously established formalism [28]. The model comprised a soma; a 140-µm-long, 0.8-µm-diameter axon; and a 200-µm-long, 1-µm-diameter dendrite. Axonal cable parameters were as follows: axon Ra = 0.8–1.1 MΩ·µm; axon Cm = 6 fF/µm^2. Dendritic Cm was set to 12 fF/µm^2, i.e., 2-fold higher than that of the axon. The somatic compartment had a resistance of 700 MΩ and a Cm of 25 pF. The leakage reversal potential was set to −68 mV. Rheobase and voltage sag parameters were chosen to match the basic response properties and carefully adjusted using the experimental data to match the simulated

1030 and recorded voltage traces. All intrinsic voltage-dependent currents were calculated using the
1031 following equation:

1032

1033 $$I_i = g_i m_i^p h_i (E_i - V),$$

1034

1035 where i represents individual current type; g_i is the maximal conductance of the current; m_i
1036 and h_i are the activation and inactivation (either first-order or absent) variables, respectively;
1037 p is the activation exponent; and E_i is the reversal potential. Activation (m) and inactivation
1038 (h) kinetics were modeled based on the following equation:

1039

1040 $$\frac{dx}{dt} = \frac{x_\infty(V) - x}{\tau_x(V)},$$

1041

1042 where x represents m or h. The voltage-dependent steady-state activation and inactivation are
1043 described by the following sigmoid function:

1044

1045 $$x_\infty(V) = \frac{1}{2} + \frac{1}{2}\tanh\left(\frac{V - V_{x,1/2}}{V_{x,sl}}\right).$$

1046

1047 The midpoint $V_{x,1/2}$ and slope $V_{x,sl}$ parameters of the sigmoids and other kinetic parameters were
1048 presented in previous study [63]. The tau (τ) values of activation and inactivation were modeled
1049 as bell-shaped functions of the Vm (V) according to the following equation:

1050

1051 $$\tau_x(V) = (\tau_{x,max} - \tau_{x,min})\left[1 - \tanh\left(\frac{V - V_{\tau x,1/2}}{V_{\tau x,sl}}\right)^2\right] + \tau_{x,min}.$$

1052 EPSP waveforms were generated by EPSCs with a time to peak of 0.5 ms, a decay time
1053 constant of 3 ms, a reversal potential of 0 mV, and peak conductances of 6–11 nS.

1054

1055 Statistical analysis

1056 Results are presented as medians and IQRs. Statistical comparisons were performed
1057 using the Student's t-test, the Mann–Whitney U test, Wilcoxon signed-rank test with
1058 Bonferroni correction, ANOVA on ranks (Kruskal–Wallis H test) with Dunn's *post hoc*
1059 pairwise test, or PERMANOVA and the Mann–Whitney U test with Bonferroni correction.
1060 Proportions were compared using the chi-squared test with Benjamini–Hochberg adjustment
1061 at a 5% significance level. Correlations were assessed using Spearman's rank-order method.

1062

1063 Acknowledgments

1064 We thank both Dr. Ferhan Ayaydin at the Functional Cell Biology and Immunology
1065 Advanced Core Facility, Hungarian Center of Excellence for Molecular Medicine, and Szeged
1066 University and Dr. Fanni Nedenyi at HCEMM for help with statistical analyses. The funders
1067 played no role in the study design, data collection and analysis, decision to publish, or
1068 preparation of the manuscript. The authors would like to thank Enago (www.enago.com) for
1069 the English language review.

1070

1071 # References

1072 1. Galakhova AA, Hunt S, Wilbers R, Heyer DB, de Kock CPJ, Mansvelder HD, et al.
1073 Evolution of cortical neurons supporting human cognition. Trends Cogn Sci. 2022;26: 909-
1074 922.
1075 2. Nehme R, Pietiläinen O, Barrett LE. Genomic, molecular, and cellular divergence of the
1076 human brain. Trends Neurosci. 2024;47: 491-505.
1077 3. Warming H, Pegasiou C-M, Pitera AP, Kariis H, Houghton SD, Kurbatskaya K, et al. A
1078 primate-specific short GluN2A-NMDA receptor isoform is expressed in the human brain.
1079 Mol Brain. 2019;12: 64.
1080 4. Herculano-Houzel S, Catania K, Manger PR, Kaas JH. Mammalian brains are made of
1081 these: a dataset of the numbers and densities of neuronal and nonneuronal cells in the brain of
1082 glires, primates, scandentia, eulipotyphlans, afrotherians and artiodactyls, and their
1083 relationship with body mass. Brain Behav Evol. 2015;86: 145-163.
1084 5. Berg J, Sorensen SA, Ting JT, Miller JA, Chartrand T, Buchin A, et al. Human neocortical
1085 expansion involves glutamatergic neuron diversification. Nature. 2021;598: 151-158.
1086 6. Hodge RD, Bakken TE, Miller JA, Smith KA, Barkan ER, Graybuck LT, et al. Conserved
1087 cell types with divergent features in human versus mouse cortex. Nature. 2019;573: 61-68.
1088 7. Zeng H, Shen EH, Hohmann JG, Oh SW, Bernard A, Royall JJ, et al. Large-scale cellular-
1089 resolution gene profiling in human neocortex reveals species-specific molecular signatures.
1090 Cell. 2012;149: 483-496.
1091 8. Suresh H, Crow M, Jorstad N, Hodge R, Lein E, Dobin A, et al. Comparative single-cell
1092 transcriptomic analysis of primate brains highlights human-specific regulatory evolution. Nat
1093 Ecol Evol. 2023;7: 1930-1943.

1094 9. Rossi F. Evolutionary mechanisms and neural adaptation: selective versus constructive
1095 strategies in the development and plasticity of the nervous system. In: Fasolo A, editor. The
1096 theory of evolution and its impact. Milano: Springer; 2012. pp. 159-174.
1097 10. Beauchamp A, Yee Y, Darwin BC, Raznahan A, Mars RB, Lerch JP. Whole-brain
1098 comparison of rodent and human brains using spatial transcriptomics. Elife. 2022;11.
1099 11. Boldog E, Bakken TE, Hodge RD, Novotny M, Aevermann BD, Baka J, et al.
1100 Transcriptomic and morphophysiological evidence for a specialized human cortical
1101 GABAergic cell type. Nat Neurosci. 2018;21: 1185-1195.
1102 12. Campagnola L, Seeman SC, Chartrand T, Kim L, Hoggarth A, Gamlin C, et al. Local
1103 connectivity and synaptic dynamics in mouse and human neocortex. Science. 2022;375:
1104 eabj5861.
1105 13. Chittajallu R, Auville K, Mahadevan V, Lai M, Hunt S, Calvigioni D, et al. Activity-
1106 dependent tuning of intrinsic excitability in mouse and human neurogliaform cells. Elife.
1107 2020;9: e57571.
1108 14. Clowry GJ. An enhanced role and expanded developmental origins for gamma-
1109 aminobutyric acidergic interneurons in the human cerebral cortex. J Anat. 2015;227: 384-
1110 393.
1111 15. Dehay C, Huttner WB. Development and evolution of the primate neocortex from a
1112 progenitor cell perspective. Development. 2024;151: dev199171.
1113 16. Heyer DB, Wilbers R, Galakhova AA, Hartsema E, Braak S, Hunt S, et al. Verbal and
1114 general IQ associate with supragranular layer thickness and cell properties of the left
1115 temporal cortex. Cereb Cortex. 2022;32: 2343-2357.
1116 17. Hu X, Rocco BR, Fee C, Sibille E. Cell type-specific gene expression of alpha 5 subunit-
1117 containing gamma-aminobutyric acid subtype A receptors in human and mouse frontal
1118 cortex. Mol Neuropsychiatry. 2019;4: 204-215.

1119 18. Jorstad NL, Song JH, Exposito-Alonso D, Suresh H, Castro N, Krienen FM, et al.
1120 Comparative transcriptomics reveals human-specific cortical features. Science. 2023;382:
1121 eade9516.
1122 19. Kalmbach BE, Buchin A, Long B, Close J, Nandi A, Miller JA, et al. h-channels
1123 contribute to divergent intrinsic membrane properties of supragranular pyramidal neurons in
1124 human versus mouse cerebral cortex. Neuron. 2018;100: 1194-1208.e5.
1125 20. Shepherd GM, Rowe TB. Neocortical lamination: insights from neuron types and
1126 evolutionary precursors. Front Neuroanat. 2017;11: 100.
1127 21. Lim L, Mi D, Llorca A, Marín O. Development and functional diversification of cortical
1128 interneurons. Neuron. 2018;100: 294-313.
1129 22. Tremblay R, Lee S, Rudy B. GABAergic interneurons in the neocortex: from cellular
1130 properties to circuits. Neuron. 2016;91: 260-292.
1131 23. Lee BR, Dalley R, Miller JA, Chartrand T, Close J, Mann R, et al. Signature
1132 morphoelectric properties of diverse GABAergic interneurons in the human neocortex.
1133 Science. 2023;382: eadf6484.
1134 24. Mihaljević B, Larrañaga P, Bielza C. Comparing the electrophysiology and morphology
1135 of human and mouse layer 2/3 pyramidal neurons with bayesian networks. Front
1136 Neuroinform. 2021;15: 580873.
1137 25. Moradi Chameh H, Rich S, Wang L, Chen FD, Zhang L, Carlen PL, et al. Diversity
1138 amongst human cortical pyramidal neurons revealed via their sag currents and frequency
1139 preferences. Nat Commun. 2021;12: 2497.
1140 26. Olah S, Komlosi G, Szabadics J, Varga C, Toth E, Barzo P, et al. Output of
1141 neurogliaform cells to various neuron types in the human and rat cerebral cortex. Front
1142 Neural Circuits. 2007;1: 4.

1143 27. Poorthuis RB, Muhammad K, Wang M, Verhoog MB, Junek S, Wrana A, et al. Rapid
1144 neuromodulation of layer 1 interneurons in human neocortex. Cell Rep. 2018;23: 951-958.
1145 28. Szegedi V, Bakos E, Furdan S, Kovács BH, Varga D, Erdélyi M, et al. HCN channels at
1146 the cell soma ensure the rapid electrical reactivity of fast-spiking interneurons in human
1147 neocortex. PLoS Biol. 2023;21: e3002001.
1148 29. Testa-Silva G, Rosier M, Honnuraiah S, Guzulaitis R, Megias AM, French C, et al. High
1149 synaptic threshold for dendritic NMDA spike generation in human layer 2/3 pyramidal
1150 neurons. Cell Rep. 2022;41: 111787.
1151 30. Verhoog MB, Goriounova NA, Obermayer J, Stroeder J, Hjorth JJ, Testa-Silva G, et al.
1152 Mechanisms underlying the rules for associative plasticity at adult human neocortical
1153 synapses. J Neurosci. 2013;33: 17197-17208.
1154 31. Wilbers R, Galakhova AA, Driessens SLW, Heistek TS, Metodieva VD, Hagemann J, et
1155 al. Structural and functional specializations of human fast spiking neurons support fast
1156 cortical signaling. Sci Adv. 2023;9: eadf0708.
1157 32. Krubitzer L. In search of a unifying theory of complex brain evolution. Ann N Y Acad
1158 Sci. 2009;1156: 44-67.
1159 33. Rich S, Moradi Chameh H, Sekulic V, Valiante TA, Skinner FK. Modeling reveals
1160 human-rodent differences in H-current kinetics influencing resonance in cortical layer 5
1161 neurons. Cereb Cortex. 2021;31: 845-872.
1162 34. Libé-Philippot B, Lejeune A, Wierda K, Louros N, Erkol E, Vlaeminck I, et al.
1163 LRRC37B is a human modifier of voltage-gated sodium channels and axon excitability in
1164 cortical neurons. Cell. 2023;186: 5766-5783.e25.
1165 35. Mertens EJ, Leibner Y, Pie J, Galakhova AA, Waleboer F, Meijer J, et al. Morpho-
1166 electric diversity of human hippocampal CA1 pyramidal neurons. Cell Rep. 2024;43: 114100.

1167 36. Povysheva NV, Zaitsev AV, Rotaru DC, Gonzalez-Burgos G, Lewis DA, Krimer LS.
1168 Parvalbumin-positive basket interneurons in monkey and rat prefrontal cortex. J
1169 Neurophysiol. 2008;100: 2348-2360.
1170 37. Wang B, Ke W, Guang J, Chen G, Yin L, Deng S, et al. Firing frequency maxima of fast-
1171 spiking neurons in human, monkey, and mouse neocortex. Front Cell Neurosci. 2016;10: 239.
1172 38. Szegedi V, Molnár G, Paizs M, Csakvari E, Barzó P, Tamás G, et al. High-precision fast-
1173 spiking basket cell discharges during complex events in the human neocortex. eNeuro.
1174 2017;4: ENEURO.0260-17.2017.
1175 39. Szegedi V, Paizs M, Baka J, Barzo P, Molnar G, Tamas G, et al. Robust perisomatic
1176 GABAergic self-innervation inhibits basket cells in the human and mouse supragranular
1177 neocortex. Elife. 2020;9: e51691.
1178 40. Hijazi S, Smit AB, van Kesteren RE. Fast-spiking parvalbumin-positive interneurons in
1179 brain physiology and Alzheimer's disease. Mol Psychiatry. 2023;28: 4954-4967.
1180 41. Huang CY, Rasband MN. Axon initial segments: structure, function, and disease. Ann N
1181 Y Acad Sci. 2018;1420: 46-61.
1182 42. Leterrier C. The axon initial segment: an updated viewpoint. J Neurosci. 2018;38: 2135-
1183 2145.
1184 43. Hu H, Gan J, Jonas P. Fast-spiking, parvalbumin(+) GABAergic interneurons: from
1185 cellular design to microcircuit function. Science. 2014;345: 1255263.
1186 44. Li T, Tian C, Scalmani P, Frassoni C, Mantegazza M, Wang Y, et al. Action potential
1187 initiation in neocortical inhibitory interneurons. PLoS Biol. 2014;12: e1001944.
1188 45. Yamada R, Kuba H. Structural and functional plasticity at the axon initial segment. Front
1189 Cell Neurosci. 2016;10: 250.
1190 46. Yang Y, Ogawa Y, Hedstrom KL, Rasband MN. βIV spectrin is recruited to axon initial
1191 segments and nodes of Ranvier by ankyrinG. J Cell Biol. 2007;176: 509-519.

1192 47. Jones SL, Svitkina TM. Axon initial segment cytoskeleton: architecture, development,
1193 and role in neuron polarity. Neural Plast. 2016;2016: 1-19.
1194 48. Goethals S, Brette R. Theoretical relation between axon initial segment geometry and
1195 excitability. Elife. 2020;9: e54342.
1196 49. Kole MH, Stuart GJ. Signal processing in the axon initial segment. Neuron. 2012;73:
1197 235-247.
1198 50. Kuba H, Ohmori H. Roles of axonal sodium channels in precise auditory time coding at
1199 nucleus magnocellularis of the chick. J Physiol. 2009;587: 87-100.
1200 51. Lorincz A, Nusser Z. Cell-type-dependent molecular composition of the axon initial
1201 segment. J Neurosci. 2008;28: 14329-14340.
1202 52. O'Brien JE, Meisler MH. Sodium channel SCN8A (Nav1.6): properties and de novo
1203 mutations in epileptic encephalopathy and intellectual disability. Front Genet. 2013;4: 213.
1204 53. Goldberg EM, Clark BD, Zagha E, Nahmani M, Erisir A, Rudy B. K+ channels at the
1205 axon initial segment dampen near-threshold excitability of neocortical fast-spiking
1206 GABAergic interneurons. Neuron. 2008;58: 387-400.
1207 54. Kole MH, Letzkus JJ, Stuart GJ. Axon initial segment Kv1 channels control axonal action
1208 potential waveform and synaptic efficacy. Neuron. 2007;55: 633-647.
1209 55. Gu C, Barry J. Function and mechanism of axonal targeting of voltage-sensitive
1210 potassium channels. Prog Neurobiol. 2011;94: 115-132.
1211 56. D'Adamo MC, Liantonio A, Rolland J-F, Pessia M, Imbrici P. Kv1.1 channelopathies:
1212 pathophysiological mechanisms and therapeutic approaches. Int J Mol Sci. 2020;21: 2935.
1213 57. Ogawa Y, Horresh I, Trimmer JS, Bredt DS, Peles E, Rasband MN. Postsynaptic density-
1214 93 clusters Kv1 channels at axon initial segments independently of Caspr2. J Neurosci.
1215 2008;28: 5731-5739.

1216 58. Higgs MH, Spain WJ. Kv1 channels control spike threshold dynamics and spike timing in
1217 cortical pyramidal neurones. J Physiol. 2011;589: 5125-5142.
1218 59. Shao M, Zhang W, Li Y, Tang L, Hao ZZ, Liu S. Patch-seq: advances and biological
1219 applications. Cell Mol Neurobiol. 2023;44: 8.
1220 60. Cadwell CR, Tolias AS. Patch-seq: multimodal profiling of single-cell morphology,
1221 electrophysiology, and gene expression. Methods Mol Biol. 2024;2752: 227-243.
1222 61. Chow A, Erisir A, Farb C, Nadal MS, Ozaita A, Lau D, et al. K(+) channel expression
1223 distinguishes subpopulations of parvalbumin- and somatostatin-containing neocortical
1224 interneurons. J Neurosci. 1999;19: 9332-9345.
1225 62. Martina M, Schultz JH, Ehmke H, Monyer H, Jonas P. Functional and molecular
1226 differences between voltage-gated K+ channels of fast-spiking interneurons and pyramidal
1227 neurons of rat hippocampus. J Neurosci. 1998;18: 8111-8125.
1228 63. Szegedi V, Tiszlavicz Á, Furdan S, Douida A, Bakos E, Barzo P, et al. Aging-associated
1229 weakening of the action potential in fast-spiking interneurons in the human neocortex. J
1230 Biotechnol. 2024;389: 1-12.
1231 64. Krubitzer L, Kaas J. The evolution of the neocortex in mammals: how is phenotypic
1232 diversity generated? Curr Opin Neurobiol. 2005;15: 444-453.
1233 65. Blekhman R, Oshlack A, Chabot AE, Smyth GK, Gilad Y. Gene regulation in primates
1234 evolves under tissue-specific selection pressures. PLoS Genet. 2008;4: e1000271.
1235 66. Vallender EJ, Mekel-Bobrov N, Lahn BT. Genetic basis of human brain evolution.
1236 Trends Neurosci. 2008;31: 637-644.
1237 67. Rosales-Reynoso MA, Juárez-Vázquez CI, Barros-Núñez P. Evolution and genomics of
1238 the human brain. Neurología. 2018;33: 254-265.
1239 68. Caglayan E, Ayhan F, Liu Y, Vollmer RM, Oh E, Sherwood CC, et al. Molecular features
1240 driving cellular complexity of human brain evolution. Nature. 2023;620: 145-153.

1241 69. Zhou Y, Song H, Ming GL. Genetics of human brain development. Nat Rev Genet.
1242 2024;25: 26-45.
1243 70. Kawaguchi Y, Kubota Y. GABAergic cell subtypes and their synaptic connections in rat
1244 frontal cortex. Cereb Cortex. 1997;7: 476-486.
1245 71.Gonchar Y, Wang Q, Burkhalter AH. Multiple distinct subtypes of GABAergic neurons in
1246 mouse visual cortex identified by triple immunostaining. Front Neuroanat. 2007;1: 3.
1247 72. Ruden JB, Dugan LL, Konradi C. Parvalbumin interneuron vulnerability and brain
1248 disorders. Neuropsychopharmacol. 2021;46: 279-287.
1249 73. Lewis DA, Curley AA, Glausier JR, Volk DW. Cortical parvalbumin interneurons and
1250 cognitive dysfunction in schizophrenia. Trends Neurosci. 2012;35: 57-67.
1251 74. Nahar L, Delacroix BM, Nam HW. The role of parvalbumin interneurons in
1252 neurotransmitter balance and neurological disease. Front Psychiatry. 2021;12: 679960.
1253 75. Marin O. Parvalbumin interneuron deficits in schizophrenia. Eur Neuropsychopharmacol.
1254 2024;82: 44-52.
1255 76. Brickley SG, Revilla V, Cull-Candy SG, Wisden W, Farrant M. Adaptive regulation of
1256 neuronal excitability by a voltage- independent potassium conductance. Nature. 2001;409:
1257 88-92.
1258 77. Hall CN, Klein-Flugge MC, Howarth C, Attwell D. Oxidative phosphorylation, not
1259 glycolysis, powers presynaptic and postsynaptic mechanisms underlying brain information
1260 processing. J Neurosci. 2012;32: 8940-8951.
1261 78. Howarth C, Gleeson P, Attwell D. Updated energy budgets for neural computation in the
1262 neocortex and cerebellum. J Cereb Blood Flow Metab. 2012;32: 1222-1232.
1263 79. McCasland JS, Hibbard LS. GABAergic neurons in barrel cortex show strong, whisker-
1264 dependent metabolic activation during normal behavior. J Neurosci. 1997;17: 5509-5527.

1265 80. Kann O, Papageorgiou IE, Draguhn A. Highly energized inhibitory interneurons are a
1266 central element for information processing in cortical networks. J Cereb Blood Flow Metab.
1267 2014;34: 1270-1282.
1268 81. Ghirardini E, Sagona G, Marquez-Galera A, Calugi F, Navarron CM, Cacciante F, et al.
1269 Cell-specific vulnerability to metabolic failure: the crucial role of parvalbumin expressing
1270 neurons in creatine transporter deficiency. Acta Neuropathol Commun. 2023;11: 34.
1271 82. Fonseca-Azevedo K, Herculano-Houzel S. Metabolic constraint imposes tradeoff between
1272 body size and number of brain neurons in human evolution. Proc Natl Acad Sci USA.
1273 2012;109: 18571-18576.
1274 83. Pontzer H, Brown MH, Raichlen DA, Dunsworth H, Hare B, Walker K, et al. Metabolic
1275 acceleration and the evolution of human brain size and life history. Nature. 2016;533: 390-
1276 392.
1277 84. Höfflin F, Jack A, Riedel C, Mack-Bucher J, Roos J, Corcelli C, et al. Heterogeneity of
1278 the axon initial segment in interneurons and pyramidal cells of rodent visual cortex. Front
1279 Cell Neurosci. 2017;11: 332.
1280 85. Hamada MS, Goethals S, de Vries SI, Brette R, Kole MH. Covariation of axon initial
1281 segment location and dendritic tree normalizes the somatic action potential. Proc Natl Acad
1282 Sci USA. 2016;113: 14841-14846.
1283 86. Ollion J, Cochennec J, Loll F, Escudé C, Boudier T. TANGO: a generic tool for high-
1284 throughput 3D image analysis for studying nuclear organization. Bioinformatics. 2013;29:
1285 1840-1841.
1286 87. Picelli S, Faridani OR, Björklund ÅK, Winberg G, Sagasser S, Sandberg R. Full-length
1287 RNA-seq from single cells using Smart-seq2. Nat Protoc. 2014;9: 171-181.

1288 88. Hennig BP, Velten L, Racke I, Tu CS, Thoms M, Rybin V, et al. Large-scale low-cost
1289 NGS library preparation using a robust Tn5 purification and tagmentation protocol. G3.
1290 2018;8: 79-89.
1291 89. Dobin A, Davis CA, Schlesinger F, Drenkow J, Zaleski C, Jha S, et al. STAR: ultrafast
1292 universal RNA-seq aligner. Bioinformatics. 2013;29: 15-21.
1293
1294 **Funding:** Project no. TKP-2021-EGA-05 was implemented with support provided by the
1295 Ministry of Culture and Innovation of Hungary from the National Research, Development, and
1296 Innovation Fund, financed under the TKP2021-EGA funding scheme (K.L). Project no. 2022-
1297 2.1.1-NL-2022-00005 was implemented with support provided by the Ministry of Culture and
1298 Innovation of Hungary from the National Research, Development, and Innovation Fund,
1299 financed under the 2022-2.1.1-NL funding scheme (K.L). Additional funding was received
1300 from the EU's Horizon 2020 research and innovation program under grant agreement no.
1301 739593 (K.L); Nemzeti Kutatási, Fejlesztési és Innovaciós Alap OTKA K 134279 and
1302 ADVANCED_150382 Magyar Tudományos Akadémia (K.L); the Hungarian Scientific
1303 Research Foundation grant number ANN-135291 (K.L); Eötvös Loránd Research Network
1304 grants ELKH-SZTE Agykérgi Neuronhálózatok Kutatócsoport and KÖ-36/2021 (G.T.);
1305 Ministry of Human Capacities Hungary (20391-3/2018/FEKUSTRAT (G.T.) and NKP 16-3-
1306 VIII-3) (G.T.); National Research, Development and Innovation Office grants GINOP 2.3.2-
1307 15-2016-00018 (G.T); Élvonal KKP 133807 (G.T.), ÚNKP-20-5 - SZTE-681 (G.T.), 2019-
1308 2.1.7-ERA-NET-2022-00038 (G.T.), TKP2021-EGA-09 (G.T.), TKP-2021-EGA-28 (G.T.).
1309 and OTKA K128863 (G.T.); National Institutes of Health awards U01MH114812 (G.T.) and
1310 UM1MH130981 (G.T.); and National Research, Development, and Innovation Office
1311 grantno. ANN_135291 (A.S.).
1312

Author contributions: Conceptualization: K.L. and V.S. Methodology: A.S., A.T., P.B., B.B., G.H., G.T., and V.B. Investigation: E.B., A.T., V.S., A.D., D.W., J.L., S.F., and A.S. Data curation: V.S., A.D., and E.B. Formal analysis: A.T., E.B., V.S., and S.F. Supervision: K.L. Project administration: K.L. and V.S. Funding acquisition: K.L., G.T., and A.S. Writing original draft: K.L. Writing review and editing: K.L.

Competing interests: The authors declare that they have no competing interests.

Data and materials availability: All data required to evaluate the conclusions drawn in this paper are provided in the main text and Supplementary Materials. All datasets and custom codes used in the study are stored at the Hungarian Center of Excellence for Molecular Medicine, Szeged, Hungary, and are available upon request from the corresponding author.

Supplementary Materials

Fig. S1. Model cell simulation incorporating AIS parameter variability, showing no difference between species.

(A) Increasing AIS Nav1.6 conductance (gNav1.6, 15–40 nS/μm^2; abscissa) progressively lowered the AP firing threshold across multiple Kv1 activity levels (0–10 nS/μm^2). AIS length = 20 μm; axon Ra = 0.8–1.1 MΩ·μm; axon diameter = 0.8 μm. (B) Proximal–distal positioning of the AIS regulated the AP firing threshold within the range observed anatomically. Simulations used square-pulse current steps to mimic Vm changes (as shown in Fig 8). (B1) Vm traces from simulations in the model cell with the

1336 AIS positioned either directly at the axon hillock (0 µm; purple) or 10 µm distally (brown), with
1337 consistent AIS length (20 µm), axon Ra (0.8–1.1 MΩ·µm), axon diameter (0.8 µm), and channel
1338 conductances (20 nS/µm^2 for Nav1.6 and Kv1). (B2) Firing threshold values plotted for AIS locations
1339 and across three Ra conditions (0.8–1.1 MΩ·µm, indicated by symbols). A more distal AIS position
1340 consistently resulted in a lower AP firing threshold, replicating the real-neuron correlation observed in
1341 Fig 3C1. (C) Heatmap shows the relationship between axon longitudinal conductance (normally
1342 reduced by axon diameter increase) and axon diameter simulating a proportional (1.3-fold) increase in
1343 both Kv1 and Nav1.6 ion conductance with increasing axon diameter, uncoupling parameters that are
1344 typically correlated in real neurons. Increasing only the Ra lowered the AP firing threshold. Conversely,
1345 increasing the ion channel conductance with an increased AIS membrane area, while keeping the
1346 channel density fixed at 20 nS/µm² for Nav1.6 and Kv1, increased the firing threshold in the model cell.
1347 This indicates the strong effect of Kv1 channels on the threshold.
1348

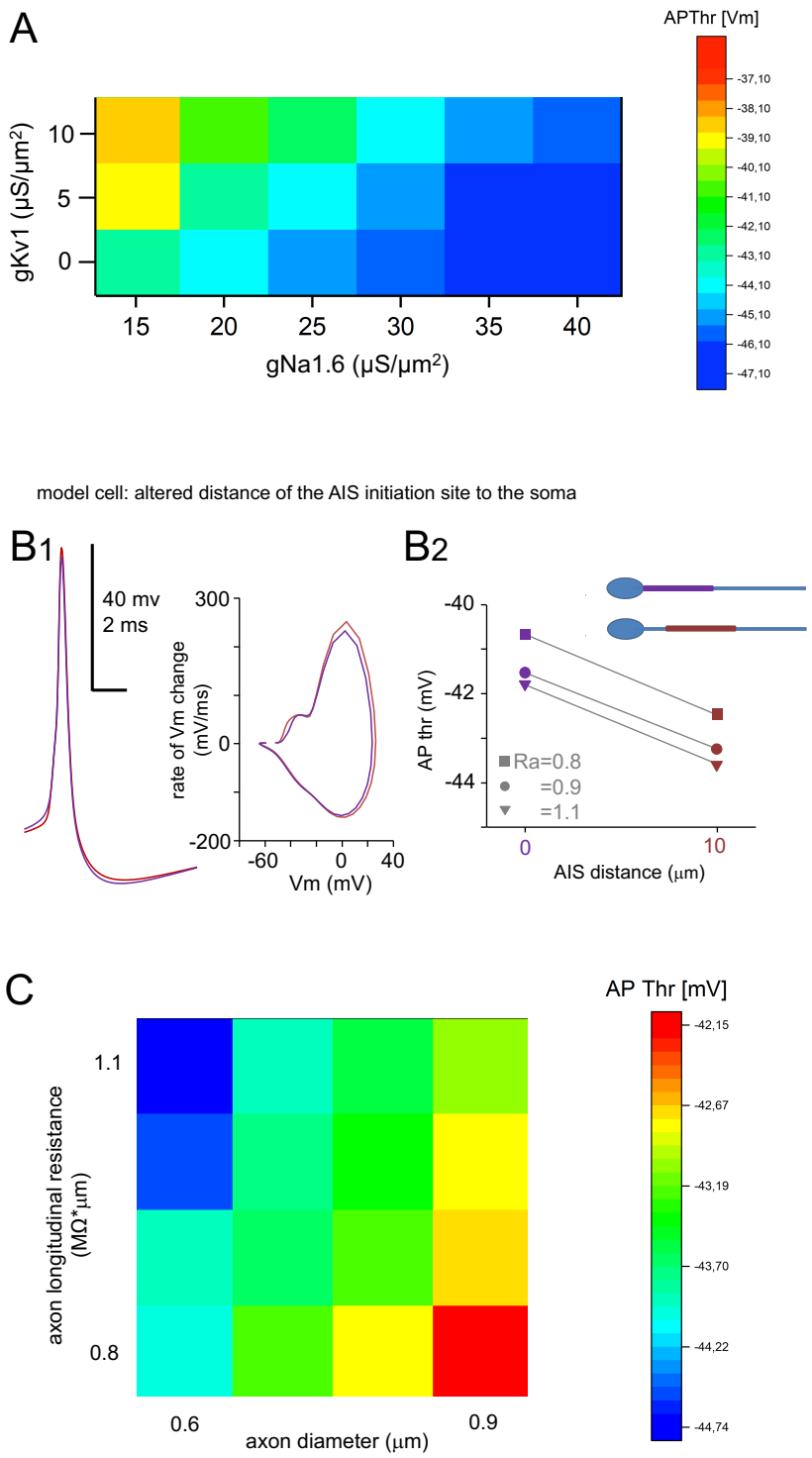

Table S1. List of neocortical pvalb cells included in the study.

cell code	pvalb+ or mRNA	AP Thr	gender	age (years)	hemisphere	region	diagnosis
h1	pvalb+	-42	F	69	right	occipital	subcortical neoplasia
h2	pvalb+	-37,3	M	38	right	temporal	malformation
h3	pvalb+	-46,8	M	38	right	temporal	malformation
h4	pvalb+	-38,5	M	66	right	temporal	tumor
h5	pvalb+	-40,1	M	45	left	frontal	tumor
h6	pvalb+	-48,2	M	21	right	parietal	tumor
h7	pvalb+	-39,1	M	21	right	parietal	tumor
h8	pvalb+	-32,9	M	40	right	frontal	tumor
h9	pvalb+	-45,6	F	70	left	parietal	hydrocephalus
h10	pvalb+	-40,2	M	69	right	parietal	hydrocephalus
h11	pvalb+	-36,8	M	58	right	frontal	tumor
h12	pvalb+	-46,1	M	58	right	frontal	tumor
h13	pvalb+	-47	F	66	right	frontal	tumor
h14	pvalb+	-26,6	F	21	right	frontal	hydrocephalus
h15	pvalb+	-27,5	no info	no info	left	parietal	tumor
h16	pvalb+	-35	F	72	right	temporobasal	tumor
h17	pvalb+	-41,3	F	72	right	temporobasal	tumor
h18	pvalb+	-46,4	M	47	left	frontotemporal	tumor
h19	pvalb+	-34,7	M	38	right	temporal	malformation
h20	pvalb+	-38,8	M	38	right	temporal	malformation
h21	pvalb+	-45,4	M	34	left	no info	malformation
h22	pvalb+	-49,1	M	11	left	temporal	malformation
h23	pvalb+	-40,5	F	61	right	frontal	tumor
h24	pvalb+	-27,9	F	17	right	parietal	tumor
h25	pvalb+	-31,2	F	65	right	frontal	colloid cysta
h26	pvalb+	-30,6	M	85	left	fronto-temporal	hydrocephalus
h27	pvalb+	-37,6	F	28	right	temporal	hydrocephalus
h28	pvalb+	-37	F	30	no info	no info	hydrocephalus
h29	pvalb+	-39,9	F	40	right	frontal	anaplastic ependymoma
h30	pvalb+	-36,8	F	40	right	frontal	anaplastic ependymoma
h31	pvalb+	-35,6	F	42	left	fronto-temporal	astrocytoma
h32	pvalb+	-39	F	78	right	frontal	hydrocephalus
h33	pvalb+	-41,1	F	68	right	temporal	hydrocephalus
h34	pvalb+	-49	F	68	right	temporal	hydrocephalus
h35	pvalb+	-38,9	F	19	right	frontal	subcortical neoplasia
h36	pvalb+	-55,8	F	19	right	frontal	subcortical neoplasia
h37	pvalb+	-52	F	50	left	occipital	astrocytoma
h38	pvalb+	-20,1	F	54	right	frontal	aneurysm
h39	pvalb+	-53,1	F	69	no info	no info	hydrocephalus
h40	pvalb+	-25,5	M	36	right	frontal	hydrocephalus
h41	pvalb+	-30	M	37	right	parietal	tumor
h42	pvalb+	-48,7	F	60	right	parietal	hydrocephalus
h43	pvalb+	-31	M	22	right	frontal	hydrocephalus
h44	pvalb+	-40,7	F	39	right	frontal	tumor
h45	pvalb+	-47,7	F	63	right	temporal	hydrocephalus
h46	pvalb+	-52,6	F	68	right	temporal	hydrocephalus
h47	pvalb+	-42,2	F	76	right	frontal	Hydrocephalus

1353

h48	pvalb+	-41,1	F	73	right	frontal	biopsy (MRI: multifocal lesions)
h49	pvalb+	-40,9	F	73	right	frontal	biopsy (MRI: multifocal lesions)
h50	pvalb+	-54	M	33	right	frontal	hydrocephalus
h51	pvalb+	-39	M	20	right	frontal	hydrocephalus
h52	pvalb+	-42,7	M	49	right	frontal	colloid cyst
h53	pvalb+	-47,6	M	66	right	frontal	astrocytoma
h54	pvalb+	-36,2	M	67	right	occipital	subcortical neoplasia
h55	pvalb+	-53,3	M	68	no info	temporal	hydrocephalus
h56	pvalb+	-45,5	M	51	no info	no info	hydrocephalus
h57	pvalb+	-38,4	F	47	right	frontal	colloid cyst
h58	pvalb+	-38,4	F	53	left	no info	tumor
h59	pvalb+	-45,9	F	30	right	frontal	tumor
h60	pvalb+	-36,4	F	30	right	frontal	tumor
h61	pvalb+	-34,8	M	41	right	parietal	shunt
h62	pvalb+	-32,3	M	20	right	temporal	tumor
h63	pvalb+	-37,7	M	43	right	frontal	tumor
h64	pvalb+	-37	M	65	right	temporal	tumor
h65	pvalb+	-35	M	65	right	temporal	tumor
h66	pvalb+	-38,5	F	67	right	parietal	shunt
h67	pvalb+	-40,6	F	55	left	temporal	tumor
h68	pvalb+	-39,3	F	79	right	parietal	hydrocephalus
h69	mRNA	-31,9	F	51	right	Insula	tumor
h70	mRNA	-25,5	M	no info	right	frontal	tumor
h71	mRNA	-42,8	M	no info	right	frontal	tumor
h72	mRNA	-28,9	M	no info	right	frontal	tumor
h73	mRNA	-26,6	M	no info	right	frontal	tumor
h74	mRNA	-21,9	M	no info	right	frontal	tumor
h75	mRNA	-32,8	M	70	left	temporal	cavernoma
h76	mRNA	-37,6	F	51	right	Insula	tumor
h77	mRNA	-31,1	F	51	right	insula	tumor
h78	mRNA	-33,9	F	51	right	insula	tumor
h79	mRNA	-40,5	M	no info	left	frontal	hydrocephalus
h80	mRNA	-32,8	M	59	right	frontal	tumor
h81	pvalb+	-19,1	F	46	right	frontal	tumor
h82	pvalb+	-18,3	F	46	right	frontal	tumor
h83	pvalb+	-26,1	F	46	right	frontal	tumor
h84	pvalb+	-34,9	M	68	left	occipital	tumor
h85	pvalb+	-43,3	M	68	left	occipital	tumor
h86	pvalb+	-41,9	M	68	left	occipital	tumor
h87	pvalb+	-43,3	F	31	left	temporal	tumor
h88	pvalb+	-37,3	M	70	right	temporal	tumor
h89	pvalb+	-40,4	M	70	right	temporal	tumor
h90	pvalb+	-34,2	M	70	right	temporal	tumor
h91	pvalb+	-38,2	M	70	right	temporal	tumor

1354